

ARTICLE

Mitophagy-mediated adipose inflammation contributes to type 2 diabetes with hepatic insulin resistance

Feng He^{1*}, Yanrui Huang^{1*}, Zhi Song^{1*}, Huanjiao Jenny Zhou^{1*}, Haifeng Zhang¹, Rachel J. Perry^{2,3}, Gerald I. Shulman^{2,3}, and Wang Min¹

White adipose tissues (WAT) play crucial roles in maintaining whole-body energy homeostasis, and their dysfunction can contribute to hepatic insulin resistance and type 2 diabetes mellitus (T2DM). However, the mechanisms underlying these alterations remain unknown. By analyzing the transcriptome landscape in human adipocytes based on available RNA-seq datasets from lean, obese, and T2DM patients, we reveal elevated mitochondrial reactive oxygen species (ROS) pathway and NF-κB signaling with altered fatty acid metabolism in T2DM adipocytes. Mice with adipose-specific deletion of mitochondrial redox *Trx2* develop hyperglycemia, hepatic insulin resistance, and hepatic steatosis. *Trx2*-deficient WAT exhibited excessive mitophagy, increased inflammation, and lipolysis. Mechanistically, mitophagy was induced through increasing ROS generation and NF-κB-dependent accumulation of autophagy receptor p62/SQSTM1, which recruits damaged mitochondria with polyubiquitin chains. Importantly, administration of ROS scavenger or NF-κB inhibitor ameliorates glucose and lipid metabolic disorders and T2DM progression in mice. Taken together, this study reveals a previously unrecognized mechanism linking mitophagy-mediated adipose inflammation to T2DM with hepatic insulin resistance.

Introduction

White adipose tissues (WAT) play crucial roles in maintaining whole-body energy homeostasis through secreting diverse metabolites and adipokines (Mottillo et al., 2016; Rutkowski et al., 2015). Human studies and animal models suggested that adipose tissue dysfunction contributes to the metabolic dysregulation associated with obesity (Bi et al., 2014; Hajer et al., 2008), hepatic insulin resistance (Mottillo et al., 2016; Tang et al., 2016), and diabetes (Hajer et al., 2008; Yang et al., 2005). Although the molecular events underlying the relationship between adipose dysfunction and these system metabolism abnormalities remain uncertain, recent studies have implicated inflammation is a potentially unifying cause (Hajer et al., 2008; Hotamisligil, 2017; Oral et al., 2017). Indeed, several studies revealed that the NF-κB transcriptional program activation is linked to the inflammatory response in adipocytes (Hajer et al., 2008; Zhao et al., 2018). Proinflammatory cytokines secreted from adipocytes not only promote insulin resistance of adipose tissue but also affect more distant sites through the circulation transportation, including the vessel walls, liver, skeletal muscle, kidneys, and circulating leukocytes (Donath and Shoelson, 2011). However, the molecular

mechanisms linking NF-κB signaling in adipocytes to hepatic insulin resistance and type 2 diabetes remain poorly understood.

Mitochondria are critical integrators of energy production, ROS generation, signaling transduction, and apoptosis (Galluzzi et al., 2012). There is increasing evidence that mitochondrial malfunction is a pivotal event in disturbing adipose homeostasis and metabolic adaptation (Kusminski and Scherer, 2012). Recent studies have demonstrated that adipose mitochondrial function and biogenesis are compromised in type 2 diabetes mellitus (T2DM; Bogacka et al., 2005), insulin resistance (Vernochet et al., 2012), and morbid obesity (Heinonen et al., 2015). As human adipose mitochondria may be targeted pharmacologically (Cypess et al., 2015; Smith et al., 2012), there is renewed interest in its therapeutic potential for treating metabolic diseases. However, the pathogenic mechanisms of adipose mitochondria resulting in systemic metabolic abnormalities have yet to be fully defined.

The thioredoxin (Trx) system is an important regulator of cellular redox state, which involves Trx, Trx reductase (TrxR), and peroxidase (Prx; Lee et al., 2013; Stanley et al., 2011). Trx's

¹Department of Pathology, Yale School of Medicine, New Haven, CT; ²Department of Cellular and Molecular Physiology, Yale School of Medicine, New Haven, CT; ³Department of Internal Medicine, Yale School of Medicine, New Haven, CT.

*F. He, Y. Huang, Z. Song, and H.J. Zhou contributed equally to this paper; Correspondence to Wang Min: mike.wang388@gmail.com; Gerald I. Shulman: gerald.shulman@yale.edu.

© 2020 He et al. This article is distributed under the terms of an Attribution–Noncommercial–Share Alike–No Mirror Sites license for the first six months after the publication date (see <http://www.rupress.org/terms/>). After six months it is available under a Creative Commons License (Attribution–Noncommercial–Share Alike 4.0 International license, as described at <https://creativecommons.org/licenses/by-nc-sa/4.0/>).

are small redox proteins (12 kD), including cytosolic Trx1 and mitochondrial Trx2, characterized by their proximate cysteines in a CXXC motif (Lee et al., 2013; Stanley et al., 2011). The mitochondrial-specific Trx2 antioxidant pathway can reduce target proteins to scavenge mitochondrial ROS by catalyzing thiol-disulfide exchange reactions (Collins et al., 2012). Global gene KO of Trx1, TrxR1, Trx2, or TrxR2 causes embryonic lethality, which is likely due to increased cellular oxidative stress (Conrad et al., 2004; Jakupoglu et al., 2005; Nonn et al., 2003; Tanaka et al., 2002). Trx1 transgene into the db/db mouse, a mouse model of T2DM, can prevent progression of hyperglycemia and the reduction of insulin content. At a molecular level, Trx1 protected pancreatic β cells from losing their insulin-secreting capacity by reducing the transcription factors expression of Pdx-1 and MafA in β cells (Yamamoto et al., 2008). The pathological function of Trx2 is less understood. Our previous studies have shown that cardiac-specific Trx2 KO mice develop spontaneous dilated cardiomyopathy, and Trx2 maintains cardiac function by inhibiting mitochondrial ROS generation and apoptosis signal-regulating kinase 1-dependent apoptosis (Huang et al., 2015). However, the role of Trx2 in adipose tissue has not been investigated.

Here, we reveal that adipose-specific Trx2 KO mice developed hepatic insulin resistance and hyperglycemia. Trx2 deficiency induced excessive mitophagy and mitochondrial structural damage, which contributed to adipose mitochondrial loss and dysfunction and further disrupted whole-body metabolic homeostasis. Mechanistically, Trx2 deficiency via ROS generation promoted NF- κ B-dependent accumulation of autophagy receptor p62/SQSTM1 to target damaged mitochondria for autophagic removal. We further show that an NF- κ B inhibitor could prevent NF- κ B/p62-mediated mitophagy and ameliorate adipose metabolic disorders and T2DM progression. Thus, Trx2 is a critical hub for integrating oxidative stress, inflammation, and mitochondrial metabolism in adipose tissue, which reveals that adipose mitophagy links NF- κ B signal activation to hepatic insulin resistance and T2DM.

Results

Adipocyte Trx2 deficiency exacerbates hyperglycemia and insulin resistance

To understand the role of adipose Trx2 in the development of metabolic diseases, we generated adipose-specific Trx2 KO (*Trx2^{ADKO}*) mice by breeding mice carrying the adiponectin promoter-Cre transgene with mice carrying floxed Trx2 alleles, which contained loxP sites flanking exon 3 (Fig. S1 A). A truncated form of Trx2 protein was not detectable, likely due to a decay of the mutant Trx2 mRNA generated upon deletion (Huang et al., 2015). Offspring that carried the floxed Trx2 alleles but were negative for the Cre transgene were used as WT controls (Fig. S1 B). As expected, Trx2 expression was greatly diminished in adipose tissue (Fig. 1 A) but was not decreased in pancreas of *Trx2^{ADKO}* mice (Fig. S1 C). *Trx2^{ADKO}* mice were viable and born at a normal Mendelian ratio but exhibited an age-dependent reduction of average body weight (Fig. S2 A). The EchoMRI scans at 14 wk of age confirmed a 10% reduction of fat

body mass in *Trx2^{ADKO}* mice (Fig. S2 B). Histological analysis of the epididymal WAT (eWAT) and inguinal WAT (ingWAT) showed that white adipocytes of *Trx2^{ADKO}* mice were smaller in size than those of WT mice, although the total adipocyte number was not significantly altered (Fig. 1 B).

To determine the reason for the diminished fat deposits in the *Trx2^{ADKO}* mice, we measured energy expenditure of the 14-wk-old mice in comprehensive laboratory animal metabolic system cages. Food intake did not differ significantly between the WT and *Trx2^{ADKO}* littermates (Fig. 1 C), whereas oxygen consumption corrected for total body weight (TBW) versus lean mass was 20% versus 16% higher in the *Trx2^{ADKO}* mice compared with WT controls ($P = 0.002$ and $P = 0.01$, respectively), which was consistent with the corresponding 19% versus 11% increase in energy expenditure in *Trx2^{ADKO}* mice ($P = 0.006$ and $P = 0.03$, respectively; Fig. S2, C and D for TBW; and Fig. 1, D and E for lean). Of note, the respiratory exchange ratio (RER) values in WT mice were >1.0 , and such a high RER (>1.0) reflected an important contribution of lipogenesis (conversion of glucose to fatty acid). The RER value in *Trx2^{ADKO}* mice was 12% to \sim 15% lower compared with controls (Fig. 1 F), suggesting that lipogenesis proceeded more slowly in *Trx2^{ADKO}* mice compared with WT mice.

To investigate the role of adipocyte Trx2 in metabolic disorders, we tested blood glucose and serum insulin levels. Blood glucose levels in both fasting and fed *Trx2^{ADKO}* mice increased with age, with an early onset of hyperglycemia at the age of 8 wk (fasting blood glucose >225 mg/dl; see Fig. 1 G for fasting and Fig. S2 F for random fed male and female mice). In addition, fasting serum insulin levels in *Trx2^{ADKO}* mice were higher compared with WT mice at young ages but declined after the age of 14 wk (Fig. 1 H) due to pancreatic damage (see below). Importantly, results of i.p. glucose and insulin tolerance tests (ITTs) at 6 wk of age, before the onset of fasting hyperglycemia, showed significant glucose intolerance and insulin resistance in *Trx2^{ADKO}* mice compared with WT controls (Fig. S2, G and H; 6 wk of age). At 14 wk of age, *Trx2^{ADKO}* mice showed a 72% and 75% increase in area under the curve (AUC) calculated from the glucose and insulin time courses, respectively (Fig. 1, I and J; 14 wk of age), indicating more severe glucose intolerance and insulin resistance. Collectively, these data suggest that white adipocyte-specific Trx2 deficiency exacerbates hyperglycemia and insulin resistance and the *Trx2^{ADKO}* mice reflect a type 2 diabetic phenotype.

We investigated whether adipose-specific Trx2 deletion affects other T2DM target organs. Hematoxylin and eosin staining and immunofluorescence analysis of the pancreas showed that pancreatic islet size and β cell content were significantly decreased in *Trx2^{ADKO}* mice compared with WT mice at 14 wk of age, and these differences were more pronounced at 24 wk (Fig. S3, A and B). We examined β cell apoptosis in *Trx2^{ADKO}* mice and found a 3.5- and 4.1-fold increase in terminal deoxynucleotidyl transferase dUTP nick end labeling (TUNEL)-positive β cells at 14 and 24 wk, respectively, compared with control mice (Fig. S3, C and D). Consistently, transmission electron microscopy (TEM) images revealed a 28% reduction in insulin granules along with many empty vesicles in β cells of 14-wk-old *Trx2^{ADKO}* mice (Fig. S3 E), indicating insufficient insulin secretion. Furthermore,

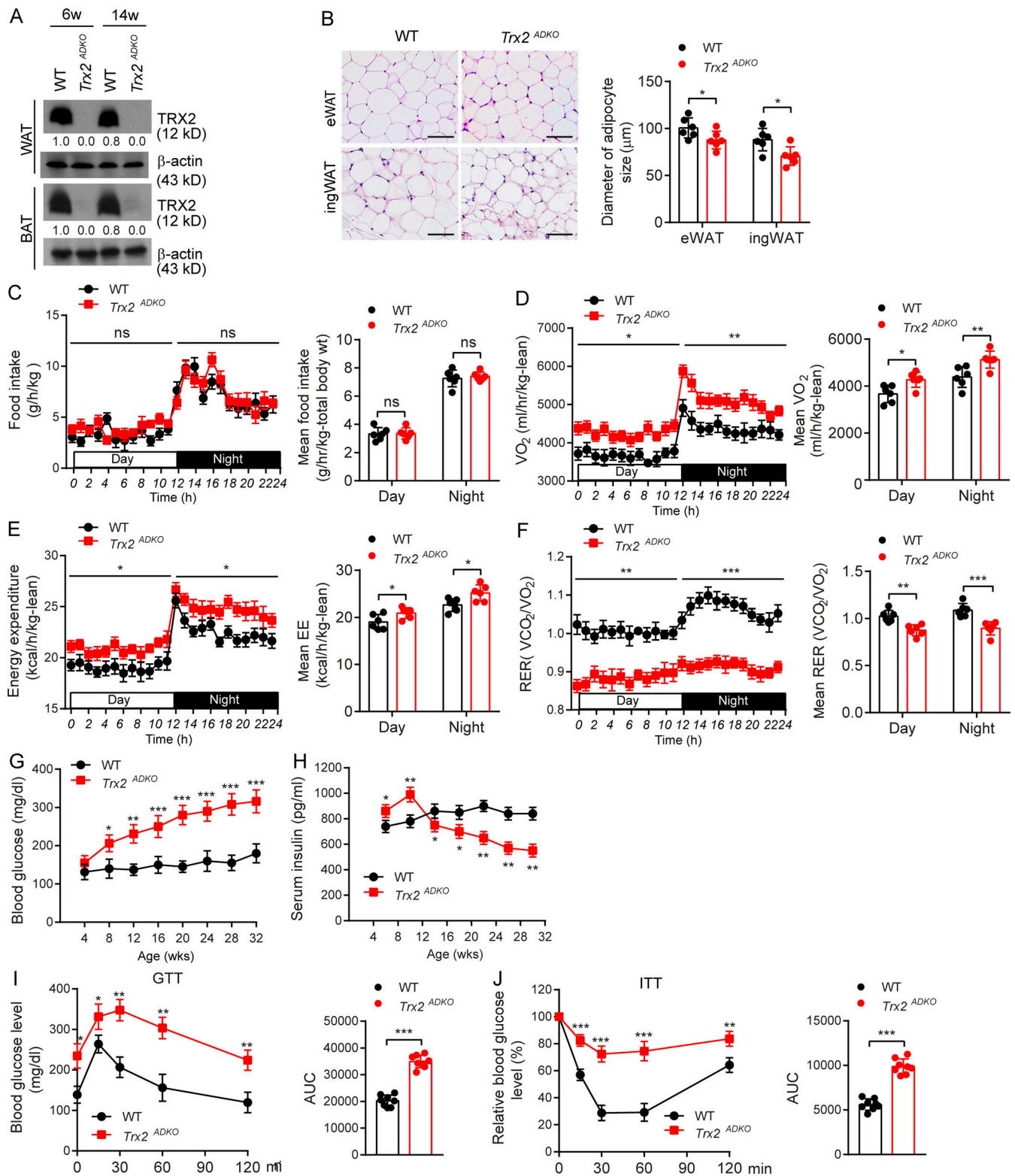


Figure 1. **Adipocyte-specific KO of Trx2 results in hyperglycemia and insulin resistance.** (A) Representative immunoblot analysis of Trx2 protein in WAT and BAT of *Trx2^{ADKO}* mice relative to the WT controls. Trx2 protein levels were quantified and presented as fold changes by taking WT as 1.0. $n = 3$ male mice. Female mice show similar Trx2 deletion. (B) Representative hematoxylin and eosin images of eWAT and ingWAT from 14-wk-old WT and *Trx2^{ADKO}* mice ($n = 6$ male). Diameters of adipocyte in eWAT and ingWAT were quantified. Female mice show similar phenotype in adipocyte size. Scale bars, 100 μ m. (C–F) Food intake, oxygen consumption corrected for lean mass, energy expenditure corrected for lean mass, and RER of 14-wk-old WT and *Trx2^{ADKO}* mice ($n = 6$). (G and H) Fasting blood glucose and serum insulin levels over time in WT and *Trx2^{ADKO}* mice ($n = 6$). (I and J) GTT and ITT in 14-wk-old male WT and *Trx2^{ADKO}* mice ($n = 8$). AUC 120 min was calculated. Quantitative data are presented as mean \pm SEM. *, $P < 0.05$; **, $P < 0.01$; ***, $P < 0.001$ versus the corresponding value for WT. Significance was analyzed by two-tailed Student's *t* test. ns, not significant.

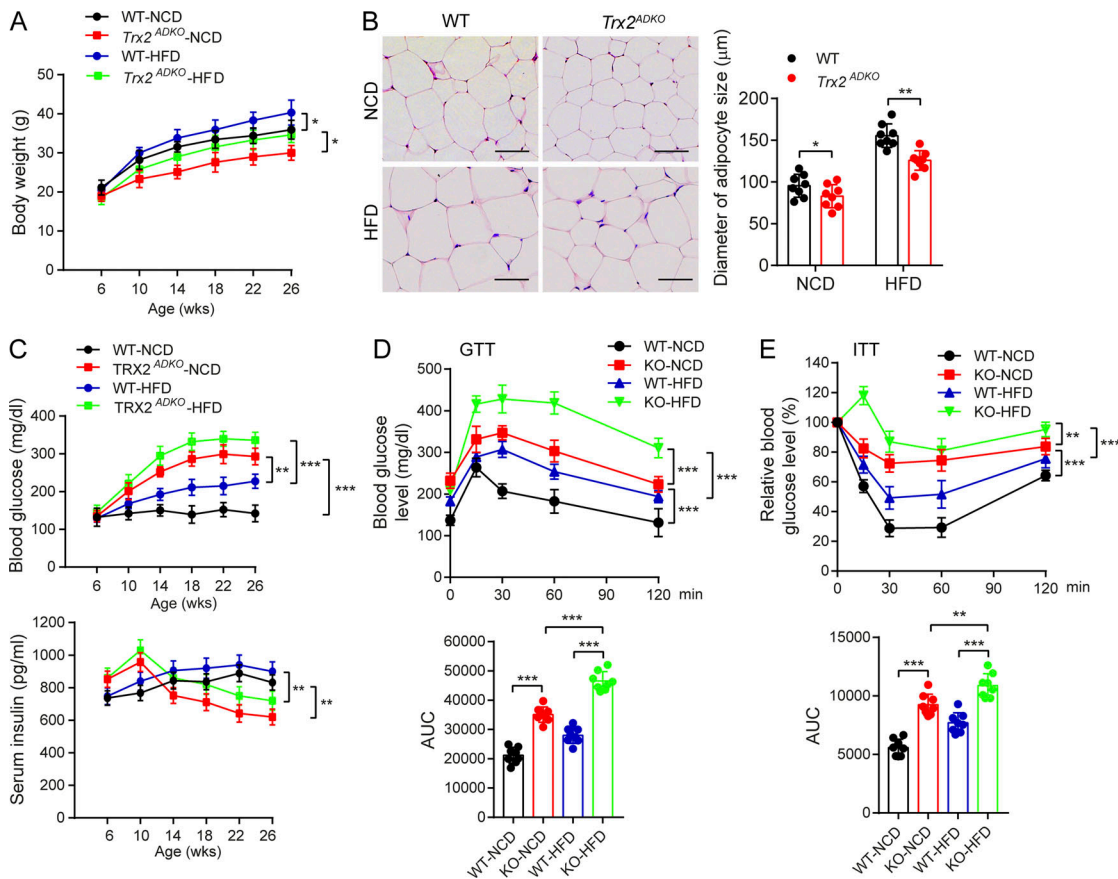


Figure 2. HFD enhances type 2 diabetic phenotype in *Trx2^{ADKO}* mice. (A) Growth curves of WT and *Trx2^{ADKO}* male mice fed the NCD or HFD ($n = 8$). (B) Hematoxylin and eosin–stained sections of eWAT from 14-wk-old WT and *Trx2^{ADKO}* mice fed the NCD or HFD for 8 wk. Diameters of adipocyte in eWAT and ingWAT were quantified. $n = 8$. Scale bars, 100 μm . (C) Fasting blood glucose levels and serum insulin levels of WT and *Trx2^{ADKO}* mice fed the NCD or HFD ($n = 8$). (D and E) GTT (D) and ITT (E) assays in 14-wk-old male WT and *Trx2^{ADKO}* mice fed the NCD or HFD for 8 wk ($n = 8$). AUC (120 min) was calculated (bottom panel). Quantitative data are presented as mean \pm SEM. *, $P < 0.05$; **, $P < 0.01$; ***, $P < 0.001$ versus the indicated comparisons. Significance was assessed by one-way ANOVA followed by Tukey’s post hoc test.

TEM images of kidney tissue showed severe podocyte foot process fusion in *Trx2^{ADKO}* mice at 14 wk of age, which is characteristic of early diabetic nephropathy and results in the disruption of the glomerular filtration barrier (Fig. S3 G). Taken together, these findings indicate that *Trx2^{ADKO}* mice developed T2DM leading to end-organ damage, as demonstrated by hyperglycemia, insulin resistance, hypertriglyceridemia, hepatic steatosis, and pancreatic and renal dysfunction.

HFD enhances the type 2 diabetic phenotype in *Trx2^{ADKO}* mice

To further determine the phenotype of *Trx2^{ADKO}* mice under high-fat diet (HFD) conditions, either a normal chow diet (NCD) or HFD were fed after weaning. Body weight of the HFD-fed *Trx2^{ADKO}* mice exhibited a 10–15% reduction than that of HFD-fed WT mice throughout HFD feeding (Fig. 2 A). Histological examination showed that white adipocytes of HFD-fed *Trx2^{ADKO}* mice were smaller than those of WT controls (Fig. 2 B). Compared with HFD-treated WT mice, *Trx2^{ADKO}* mice fed either the HFD or NCD had higher fasting blood glucose levels. Similar to the NCD data, serum insulin levels in HFD-fed *Trx2^{ADKO}* mice were higher compared with WT mice at young ages but declined after age 14 wk (Fig. 2 C). HFD-fed *Trx2^{ADKO}* mice showed more

severe glucose intolerance and insulin resistance, as indicated by blood glucose concentrations during glucose and ITTs, compared with HFD-fed WT mice (Fig. 2, D and E). Taken together, these results indicate that the HFD enhances the type 2 diabetic phenotype in *Trx2^{ADKO}* mice.

Adipocyte-specific *Trx2* deletion promotes hepatic steatosis with increased hepatic lipogenesis and gluconeogenesis

Adipocyte dysfunction accelerates ectopic lipid deposition, then contributes to insulin resistance (He et al., 2003; Lotta et al., 2017; Samuel et al., 2007; Vatner et al., 2015). To test whether *Trx2* deletion increases ectopic lipid deposition, we evaluated the liver and skeletal muscle. On gross examination, lipid depots were observed in the livers of *Trx2^{ADKO}* mice after HFD feeding for 8 wk (Fig. 3 A), and liver weight as a percentage of body weight was higher in *Trx2^{ADKO}* mice fed either the NCD or HFD compared with WT mice (Fig. 3 B), indicating ectopic lipid deposition in the liver of *Trx2^{ADKO}* mice. Hepatic steatosis is associated with metabolic syndrome and elevated serum triglyceride (TG) levels (Birkenfeld and Shulman, 2014; Samuel and Shulman, 2018). We found that hepatic TG concentrations were higher in both NCD-fed *Trx2^{ADKO}* mice (3.2-fold) and HFD-fed *Trx2^{ADKO}* mice

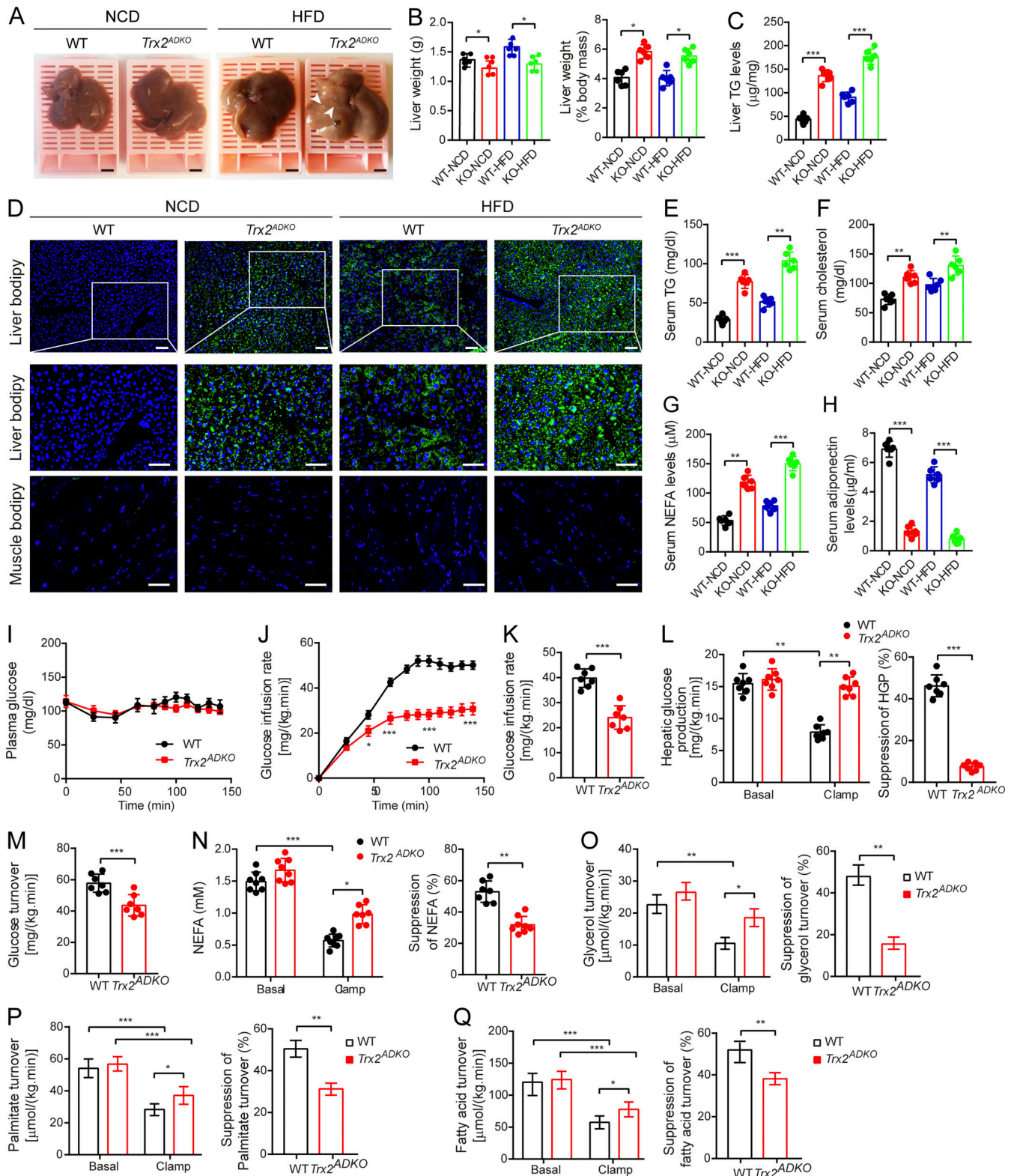


Figure 3. Adipocyte-specific *Trx2* KO promotes hepatic steatosis and hepatic insulin resistance. (A) Representative photograph of livers from 14-wk-old male WT and *Trx2*^{ADKO} mice fed the NCD or HFD for 8 wk (*n* = 6). Arrowheads indicate visible lipid deposition. Scale bars, 2 mm. (B) Liver weight and liver weight to body weight ratios of WT and *Trx2*^{ADKO} mice (KO) mice. (C) Liver TG content of mice. (D) Representative images of BODIPY staining of liver and quadriceps muscle from 14-wk-old male WT and *Trx2*^{ADKO} mice fed the HFD for 8 wk (*n* = 6). Squares correspond to the magnified areas (middle panel). Scale bars, 50 μ m. (E–H) Serum concentration of TG (E), cholesterol (F), NEFA (G), and adiponectin (H) in WT and *Trx2*^{ADKO} mice (*n* = 6). (I–Q) The hyperinsulinemic-euglycemic clamp study from WT and *Trx2*^{ADKO} mice (*n* = 7). (I) A steady plasma glucose is shown. (J) Levels of glucose after external infusion. (K) Glucose infusion rate required to maintain euglycemia during the final 40 min of the clamp. (L) Hepatic glucose production and suppression of HGP under basal and

insulin-stimulated (clamp) conditions. **(M)** Insulin-stimulated whole-body glucose uptake. **(N)** Plasma NEFA concentrations and suppression of NEFA under basal and insulin-stimulated (clamp) conditions. **(O–Q)** Lipolysis with decreased suppression of glycerol, palmitate, and fatty acid turnover under basal and insulin-stimulated (clamp) conditions. Quantitative data are shown as mean \pm SEM. *, $P < 0.05$; **, $P < 0.01$; ***, $P < 0.001$ versus the indicated comparisons. Significance was established using one-way ANOVA followed Tukey's post hoc test (B, C, and E–H) and two-tailed Student's *t* test (I–Q).

(2.0-fold) compared with their respective WT controls (Fig. 3 C). Consistent with those results, boron-dipyrromethene (BODIPY) staining revealed substantially increased lipid accumulation in livers of NCD-fed and HFD-fed *Trx2^{ADKO}* mice than in respective control mice, whereas lipid deposition in the skeletal muscle showed no significant difference between groups (Fig. 3 D). Serum TG and cholesterol levels in the *Trx2^{ADKO}* mice were also 2.8-fold and 1.6-fold higher than in WT mice, respectively, and were further elevated by the HFD (Fig. 3, E and F). Additionally, the HFD not only increased serum nonesterified fatty acid (NEFA) levels by 1.3-fold but also decreased serum adiponectin levels by 52% in *Trx2^{ADKO}* mice compared with the NCD (Fig. 3, G and H). These data demonstrated that *Trx2^{ADKO}* mice developed significant hepatic steatosis and metabolic abnormalities.

To better evaluate insulin action, NC-fed *Trx2^{ADKO}* and WT mice were subjected to hyperinsulinemic-euglycemic clamp studies. During hyperinsulinemic-euglycemic clamp, the glucose infusion rate required to maintain euglycemia was 42% lower in *Trx2^{ADKO}* mice than in WT mice (Fig. 3, I–K), demonstrating a striking decrease in whole-body insulin sensitivity. The difference in whole-body insulin sensitivity was attributed to decreased hepatic insulin responsiveness, as reflected by only 12% suppression of hepatic glucose production (HGP) during the hyperinsulinemic-euglycemic clamp in the *Trx2^{ADKO}* mice compared with 52% suppression in the WT mice. Therefore, insulin's acute ability to suppress HGP was reduced by 71% in *Trx2^{ADKO}* mice compared with controls (Fig. 3 L). Additionally, insulin-stimulated whole-body glucose uptake was reduced by 23% (Fig. 3 M) in *Trx2^{ADKO}* mice. Insulin's ability to suppress WAT lipolysis is critical for the suppression of HGP by reducing fatty acid flux to the liver (Perry et al., 2015). Consistent with this finding, we observed insulin's ability to suppress plasma NEFA concentrations during the hyperinsulinemic-euglycemic clamps was significantly impaired in the *Trx2^{ADKO}* mice (Fig. 3 N), which was associated with increased plasma NEFA concentration. Furthermore, *Trx2^{ADKO}* mice exhibited decreased suppression of glycerol, palmitate, and fatty acid turnover compared with WT mice (Fig. 3, O–Q), demonstrating that *Trx2* deletion impaired suppression of WAT lipolysis.

To understand the mechanisms underlying hepatic steatosis in *Trx2^{ADKO}* mice, we examined the expression of genes related to hepatic lipid regulation. Interestingly, the livers of *Trx2^{ADKO}* mice showed an approximately threefold increase in expression of acetyl coenzyme A (acetyl-CoA) carboxylase 1 (a lipogenesis enzyme that converts acetyl-CoA to malonyl-CoA) and fatty acid synthase (FASN; an enzyme converts malonyl-CoA to saturated long-chain fatty acids). However, the lipoprotein lipase (*Lpl*) gene, which is involved in lipid uptake, was not altered in *Trx2^{ADKO}* mice (Fig. S3 H), indicating that a de novo fatty acid synthesis related hepatic steatosis in *Trx2^{ADKO}* mice. We also

examined genes involved in hepatic glycogen synthesis and gluconeogenesis, and observed 29% lower glycogen synthase 2 (*Gys2*) gene expression and 3.0-fold higher pyruvate carboxylase (*Pc*) gene expression in the livers of *Trx2^{ADKO}* mice compared with controls (Fig. S3 I). This finding, in the setting of the observed increase in fasting plasma glucose concentrations in *Trx2^{ADKO}* mice, suggests that hepatic gluconeogenesis was increased, but hepatic glycogen synthesis was decreased, in *Trx2^{ADKO}* mice. The livers of *Trx2^{ADKO}* mice also showed 2.4-fold higher expression of glucose 6-phosphatase (*G6p*), which encodes the enzyme catalyzing the terminal step of glycogenolysis and gluconeogenesis, and 34% lower expression of glucokinase (*Gck*), which catalyzes the initial step in hepatic utilization of glucose (Fig. S3 J). Taken together, these findings suggest that adipose-specific *Trx2* deletion promotes hepatic gluconeogenesis and lipogenesis, which promotes hepatic steatosis and hyperglycemia.

Adipocyte-specific *Trx2* deletion induces excessive mitophagy in WAT with disrupted metabolic homeostasis

Because *Trx2* deletion was adipose tissue specific, the observed systemic and liver phenotypes in *Trx2^{ADKO}* mice should be attributed to the function of *Trx2* in the adipose tissues. An important question is whether *Trx2* deletion disrupts metabolic homeostasis in adipose tissue in vivo. Consistent with the observation in Fig. 3 G, *Trx2^{ADKO}* mice exhibited higher levels of NEFA at various ages (Fig. 4 A). In contrast, *Trx2^{ADKO}* mice had significantly lower serum levels of the adipokines adiponectin and leptin (Fig. 4, B and C). Compared with WT mice, *Trx2^{ADKO}* mice showed elevated expression of genes encoding the lipolysis enzymes adipose TG lipase and hormone-sensitive lipase (HSL) in eWAT (Fig. S3 K). In addition, *Trx2^{ADKO}* mice showed decreased expression of genes encoding the lipogenesis enzymes ACC1 and FASN (Fig. S3 L). These data were consistent with less fat mass and increased plasma NEFA levels observed in *Trx2^{ADKO}* mice.

Because WAT function can be impaired by altering mitochondrial structure or oxidative capacity (Guilherme et al., 2008; Kusminski and Scherer, 2012; Zhang et al., 2010), mitochondrial dysfunction in adipocytes is directly linked to metabolic disorders such as T2DM and insulin resistance. The main function of mitochondria is to produce usable energy in the form of ATP by oxidizing glucose and lipids. The tricarboxylic acid cycle and oxidative phosphorylation (OXPHOS) are the two central metabolic pathways (Fig. 4 D). To assess the metabolic function of mitochondria, we evaluated the expression of tricarboxylic acid cycle enzymes and the five OXPHOS complexes. *Trx2^{ADKO}* white adipocytes showed lower levels of the key tricarboxylic acid cycle enzymes CIT1, IDH1, and KGD1 compared with WT white adipocytes and lower levels of OXPHOS complexes I, II, III, and IV (Fig. 4 E). Consistent with those results, *Trx2* deletion also

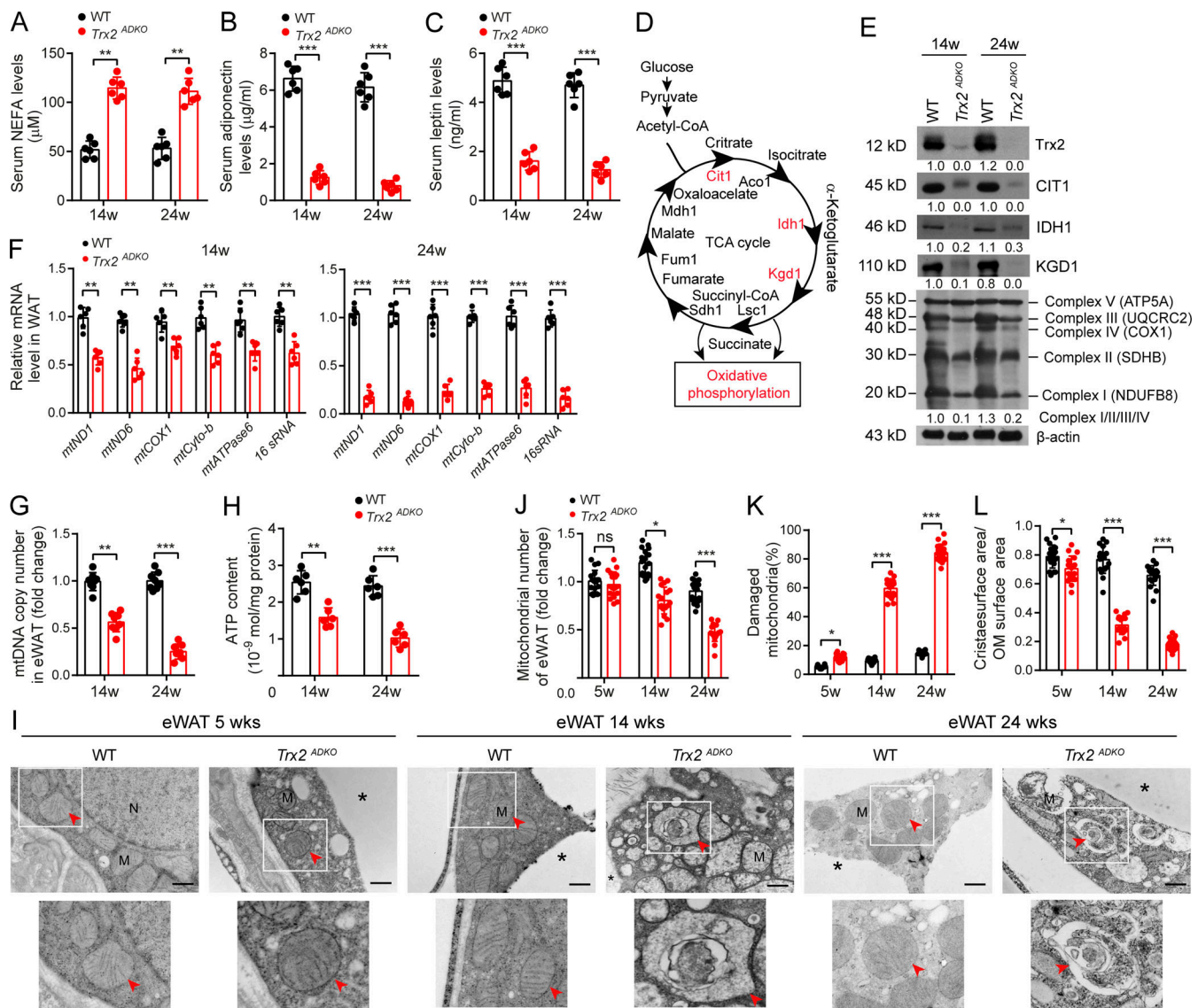


Figure 4. Adipocyte-specific Trx2 KO results in severe mitophagy and mitochondrial dysfunction. (A–C) Serum levels of NEFA (A), adiponectin (B), and leptin (C) in WT and *Trx2^{ADKO}* mice ($n = 6$). (D) Diagram of tricarboxylic acid (TCA) cycle and OXPHOS. Cit1 (citrate synthase), Idh1 (isocitrate dehydrogenase), Kgd1 (α -ketoglutarate dehydrogenase), Lsc1 (succinyl-CoA ligase), Sdh1 (succinate dehydrogenase), Fum1 (fumarase), and Mdh1 (mitochondrial malate dehydrogenase). (E) Immunoblot analysis of Trx2 and rate-limiting enzymes of the tricarboxylic acid cycle and OXPHOS complexes I–V from WT and *Trx2^{ADKO}* mice. Protein levels were quantified and presented as fold changes by taking WT as 1.0. $n = 4$ mice for each group. (F) Real-time PCR analysis of mitochondrial genes in eWAT from WT and *Trx2^{ADKO}* mice at 14 and 24 wk ($n = 8$). (G) Mitochondrial DNA content in eWAT of WT and *Trx2^{ADKO}* mice ($n = 8$). (H) ATP content of mitochondria isolated from eWAT of WT and *Trx2^{ADKO}* mice ($n = 6$). (I) Representative transmission electron micrographs of eWAT sections from WT and *Trx2^{ADKO}* mice at 5, 14, and 24 wk (six images/mouse, $n = 3$ mice/group). Asterisks indicate LDs. Arrowheads indicate mitochondria. Scale bars, 0.5 μ m. Squares correspond to the magnified areas (bottom panel). (J–L) Quantification of total number of mitochondria, damaged mitochondria, and ratio of cristae surface area/outer membrane (OM) surface area (six images/mouse, $n = 3$ mice/group). Quantitative data are presented as mean \pm SEM. ns, not significant; *, $P < 0.05$; **, $P < 0.01$; ***, $P < 0.001$ for the indicated comparisons (two-tailed Student's t test). w, weeks.

resulted in progressively lower mitochondrial gene expression, mitochondrial DNA copy number, and ATP production in adipocytes (Fig. 4, F–H).

We then used TEM to assess mitochondria in the eWAT of WT and *Trx2^{ADKO}* mice, which showed that adipocyte mitochondria of WT mice were aligned in rows, whereas the adipocyte mitochondria of *Trx2^{ADKO}* eWAT displayed irregular shapes and disrupted cristae at 5 wk of age (Fig. 4 I). We observed severe mitochondrial damage and distinct mitophagy in

the eWAT of *Trx2^{ADKO}* mice at 14 wk and extensive mitophagy at 24 wk (Fig. 4 I). This result is consistent with a progressive decrease in the number of total mitochondria with an increase in the percentage of damaged mitochondria in which cristae surface areas were decreased (Fig. 4, J–L). Additionally, we did not find mitophagy in the brown adipose tissue (BAT) of *Trx2^{ADKO}* mice. However, similar mitochondrial abnormalities, including cristae disruption and mitochondrial fragmentation, were observed in the BAT of *Trx2^{ADKO}* mice (Fig. S3, M–P). These results

suggest that Trx2 plays an important role in maintaining normal mitochondrial structure and function in adipose tissue.

Collectively, these data suggest that Trx2 deficiency causes mitochondrial structure damage and excessive mitophagy, which contributes to mitochondrial dysfunction and loss, resulting in disrupted metabolic homeostasis in adipose tissue.

Trx2 deficiency induces mitochondrial ROS production and activates NF- κ B signaling in WAT

The observations above prompted us to define the mechanism by which Trx2 deletion specifically induced mitophagy in WAT. Damaged mitochondria undergo fission and segregation before removal via mitophagy (Galluzzi et al., 2012). As expected, Trx2 deficiency showed lower levels of the mitochondrial fusion-related proteins mitofusin 1 (MFN1) and optic atrophy 1 (OPA1) and higher levels of mitochondrial fission-related proteins, including dynamin-related protein 1 (Drp1) and fission 1 (Fis1; Fig. 5 A), suggesting altered mitochondrial dynamics. Consistent with TEM results showing severe mitochondrial damage in Trx2^{ADKO} eWAT, levels of the autophagy-related proteins light chain 3 (LC3) and Beclin-1 were notably increased (Fig. 5 B). Trx2^{ADKO} mice also showed increased protein levels of the autophagy receptor p62/SQSTM1, which interacts with ubiquitin and LC3 during mitophagy, whereas the protein level of neighbor of BRCA1 gene 1 (NBR1), another autophagy receptor and a functional homologue of p62, was similar to that of WT controls. These data suggest that the excessive mitophagy in Trx2^{ADKO} eWAT could be p62/SQSTM1 dependent.

Expression of p62/SQSTM1 is regulated by stress stimuli such as oxidative stress and inflammation. Using the mitochondrial superoxide indicator mitoSOX, we found that ROS generation was significantly increased by 9.0-fold in Trx2^{ADKO} eWAT at 14 wk and 6.2-fold at 24 wk compared with WT mice (Fig. 5 C). In addition, dimerization of Trx2-dependent Prx3 (Fig. 5 D), an indicator of oxidative stress (Collins et al., 2016), was significantly increased in the eWAT of Trx2^{ADKO} mice. Because excessive ROS impaired mitochondrial function, we evaluated whether metabolic function in adipocytes was impaired in Trx2^{ADKO} mice. We found that protein levels of glucose transporter type 4 (Glut4) and peroxisome proliferator-activated receptor (PPAR γ) were significantly decreased, whereas HSL protein level was increased (Fig. 5 D).

Mitochondrial ROS can activate NF- κ B signaling (Morgan and Liu, 2011; Nathan and Cunningham-Bussell, 2013), and we investigated whether Trx2 deletion activates NF- κ B signaling in Trx2^{ADKO} adipocytes. Immunoblot analysis showed increased phosphorylation of I κ B kinase (IKK), I κ B α , and NF- κ B subunit P65/RelA with a concomitant reduction of total I κ B α in Trx2^{ADKO} eWAT. However, Trx2 deletion had no effect on the levels of total and phosphorylated AKT in adipose tissues (Fig. 5 E). Furthermore, compared with controls, immunostaining of phospho-P65/RelA was significantly increased in Trx2^{ADKO} adipocyte nucleus (Fig. 5 F). However, phospho-P65/RelA did not localize with the macrophage marker F4/80 (Fig. 5 G), confirming that NF- κ B activation is adipocyte specific. Increased NF- κ B signaling is associated with the proinflammatory response (Wellen and Hotamisligil, 2005). TNF- α and IL-6 protein

levels in Trx2^{ADKO} mice were significantly higher than those of controls in both WAT and serum (Fig. 5, H and I). These data suggested that Trx2 deficiency in adipose tissue increases mitochondrial ROS generation and NF- κ B activation, inducing systemic cytokine production and disruption of whole-body glucose and lipid metabolism.

Trx2 deficiency promotes mitophagy through NF- κ B-dependent p62/SQSTM1 recruitment to mitochondria

To define the association of ROS-NF- κ B and increased p62/SQSTM1 expression in Trx2 deletion-induced mitophagy in WAT, we isolated preadipocytes from WT and Trx2^{ADKO} mice followed by differentiation in vitro (Fig. S4 A). In cultured Trx2^{ADKO} adipocytes, Trx2 protein level decreased gradually during differentiation and was >90% lower than that of WT adipocytes at day 4, whereas Trx2 protein in Trx2^{ADKO} adipocytes infected with Cre-expressing adenovirus was barely detectable at day 0 (Fig. S4 B). Therefore, we selected WT and Trx2^{ADKO} adipocytes at different time points during differentiation to investigate the effect of Trx2 deficiency on mitochondrial dynamics and mitophagy. Of note, in vitro-differentiated adipocytes contain multitudes of small (multilocular), but not unilocular, lipid droplets (LDs), as assessed by BODIPY staining. Nevertheless, we found that Trx2^{ADKO} adipocytes cells had smaller LDs and less lipid accumulation, consistent with the in vivo observations that Trx2 KO WAT has less fat mass (Fig. S4, C and D), indicating a suitable model for WAT adipocytes. Moreover, Trx2 KO resulted in a four- to sevenfold increase in mitochondrial ROS generation from day 4 to day 12, and mito-TEMPO, a specific scavenger of mitochondrial superoxide, completely cleared mitochondrial ROS (Fig. S4, E and F).

We then examined mitochondrial energetics and oxidative metabolism in WT and Trx2-KO adipocytes. ATP contents of mitochondria from WT and Trx2^{ADKO} adipocytes were measured, and Trx2^{ADKO} adipocytes had reduced mitochondrial ATP generation during differentiation (Fig. S4 G). Confocal immunofluorescence microscopy showed that Trx2 deletion promoted mitochondrial fission and mitochondrial loss over time (Fig. S4, H and I). Consistent with this result, Trx2^{ADKO} adipocytes showed a gradual decrease in the mitochondrial fusion-related proteins MFN1 and OPA1 and an increase in the mitochondrial fission-related proteins Drp1 and Fis1 (Fig. S4 J). Mitochondrial fission has been shown to result in mitochondrial membrane depolarization (Baixauli et al., 2011). Accordingly, we observed mitochondrial membrane depolarization in Trx2^{ADKO} adipocytes at day 4, as assessed by JC-1 fluorescent dye (Fig. S4 K). Next, we analyzed mitochondrial function using the Seahorse XF24 Analyzer, which showed that Trx2 KO decreased basal oxygen consumption rate, ATP-linked oxygen consumption, and reserve capacity (Fig. S4 L). Taken together, these data indicate that Trx2 KO disrupts mitochondrial dynamics, which not only reduces mitochondrial membrane potential ($\Delta\Psi$ m) and energy production but also results in mitochondrial loss.

We then investigated whether the aberrant mitochondria in Trx2^{ADKO} adipocytes could be removed by selective mitophagy. TEM results showed that Trx2^{ADKO} adipocytes exhibited typical autophagic vacuoles engulfing damaged mitochondria and a 78%

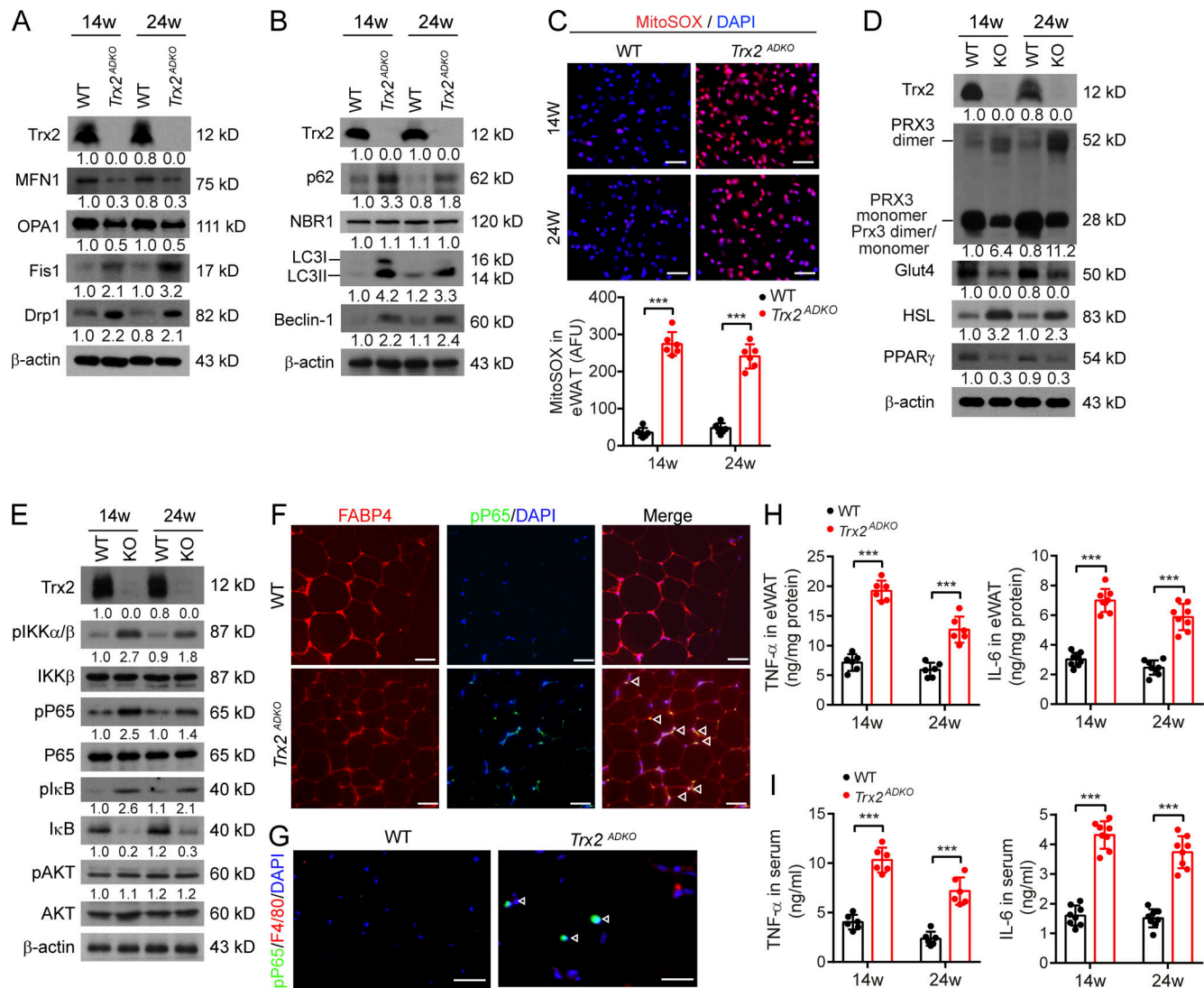


Figure 5. *Trx2* deficiency increases mitochondrial ROS generation and NF- κ B activation. (A and B) Immunoblot analysis of proteins involved in mitochondrial dynamics and mitophagy in eWAT of WT and *Trx2^{ADKO}* mice at 14 and 24 wk ($n = 3$). β -Actin was used as a loading control. **(C)** Representative micrographs of eWAT sections showing ROS levels, as assessed by the mitochondrial-specific ROS probe mitoSOX, and quantification of fluorescence intensity in WT and *Trx2^{ADKO}* mice at 14 and 24 wk ($n = 6$). AFU, arbitrary fluorescence unit. **(D)** Representative Western blot showing protein levels of Trx2, Prx3, Glut4, HSL, and PPAR γ in eWAT from WT and *Trx2^{ADKO}* mice at 14 and 24 wk. **(E)** Immunoblot analysis of IKK–NF- κ B signaling molecules (phospho-IKK α/β , IKK β , phospho-P65, P65, phospho-I κ B, I κ B, phospho-AKT, and AKT) in eWAT from WT and *Trx2^{ADKO}* mice at 14 and 24 wk. Protein levels (A, B, D, and E) were quantified and presented as fold changes by taking WT as 1.0. $n = 3$ mice for each group. **(F)** Coimmunostaining of phospho-P65 (green) and adipocyte marker FABP4 (red) in eWAT sections from 14-wk-old male WT and *Trx2^{ADKO}* mice ($n = 6$). White arrowheads indicate phospho-p65 in the nucleus. **(G)** Coimmunostaining of P65 (green) and macrophage marker F4/80 (red) in eWAT sections from 14-wk-old male WT and *Trx2^{ADKO}* mice. **(H and I)** Quantification of TNF- α and IL-6 in eWAT and serum of WT and *Trx2^{ADKO}* mice at 14 and 24 wk ($n = 8$). Data are presented as mean \pm SEM. **, $P < 0.01$; ***, $P < 0.001$ for the indicated comparisons. Significance was assessed by two-tailed Student's t test. Scale bars, 50 μ m (C); 20 μ m (F and G). w, weeks.

increase in damaged mitochondria at day 8 (Fig. 6, A and B). Consistent with the in vivo results, levels of p62 and autophagy protein components LC3II and Beclin-1 were increased at day 4 of differentiation, and gradually decreased thereafter. However, NBR1 protein level in *Trx2^{ADKO}* adipocytes was similar between the control and *Trx2*-deficient adipocytes (Fig. 6 C). Analysis of isolated mitochondria showed similar changes of these mitophagy-related markers in the mitochondria of *Trx2^{ADKO}* adipocytes at day 4 (Fig. 6 D). Induction of mitochondrial polyubiquitination appears to depend on the E3 ligase Parkin, which is activated by PTEN-induced putative

kinase 1 (PINK1) in damaged mitochondria (Matsumoto et al., 2011; Narendra et al., 2010). The *Trx2^{ADKO}* adipocytes showed p62 accumulation in the mitochondria, accompanied by an increase in the mitochondrial damage sensor (PINK1), the signal amplifier (Parkin), and autophagic vesicle expansion-associated protein ATG7 (Fig. 6 E).

Because mitochondrial ROS can activate NF- κ B signaling (Morgan and Liu, 2011; Nathan and Cunningham-Bussell, 2013), we tested whether mitochondrial ROS-activated NF- κ B signaling regulates mitophagy in *Trx2^{ADKO}* adipocytes by pharmacological inhibitors. Treatment with the mitochondrial ROS scavenger

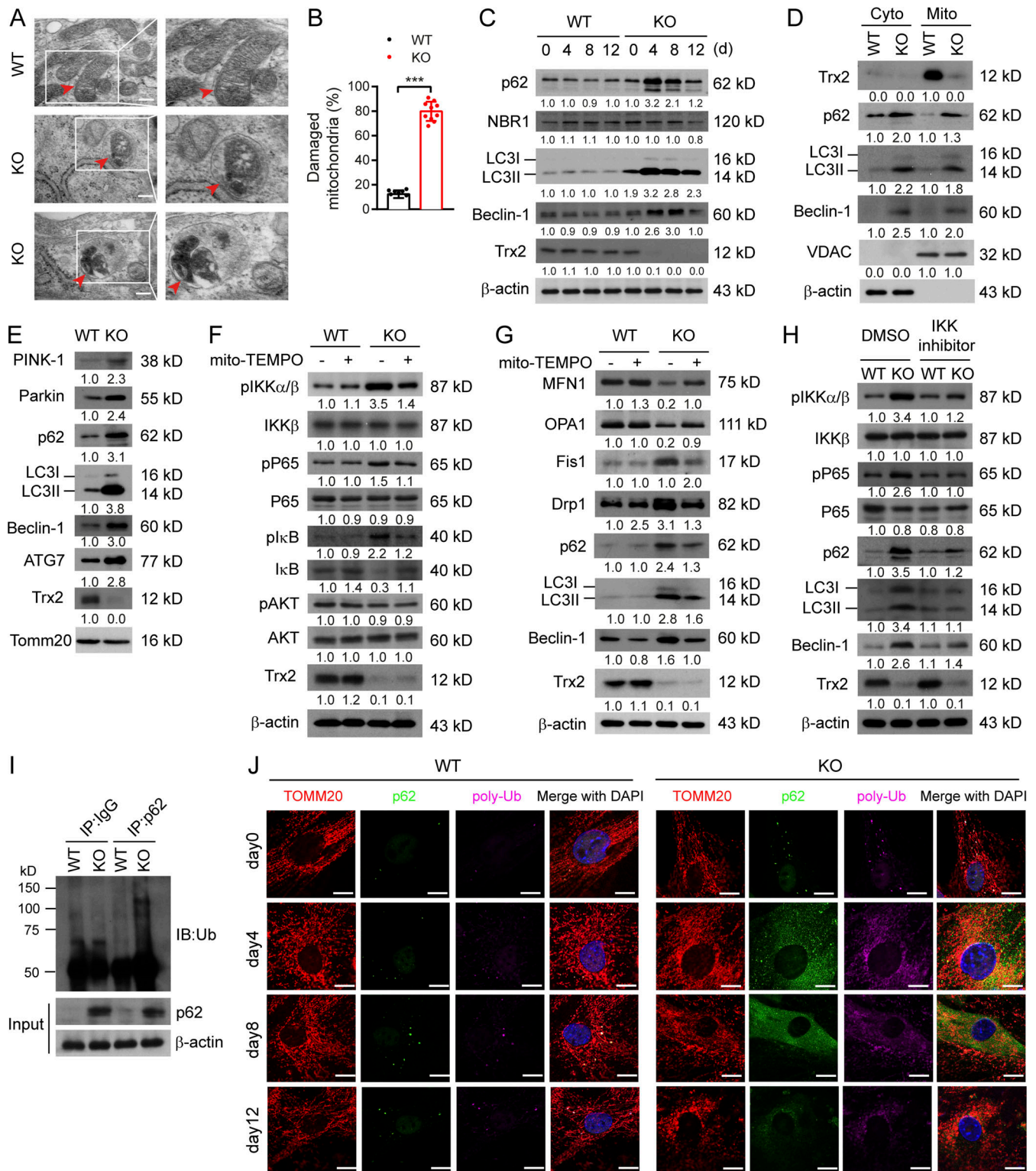


Figure 6. **Trx2** deficiency promotes mitophagy through NF-κB-dependent p62/SQSTM1 accumulation and mitochondrial recruitment. **(A)** Representative transmission electron micrographs showing typical mitophagy in differentiated adipocytes of *Trx2^{ADKO}* mice on day 8 (*n* = 3 mice/group). Squares correspond to the magnified areas. Arrows indicate mitochondria. Scale bars, 1 μm. **(B)** Percentage of damaged mitochondria in 10 random fields (*n* = 20 cells/group). **(C)** Immunoblot analysis of Trx2, mitophagy receptors p62 and NBR1, and autophagy markers LC3 and Beclin-1 in differentiated adipocytes of WT and *Trx2^{ADKO}* mice during differentiation. **(D)** Subcellular distribution of p62, LC3, and Beclin-1 in differentiated adipocytes of WT and *Trx2^{ADKO}* mice at day 4. Voltage-dependent anion channel was used as a mitochondrial control. **(E)** Immunoblot analysis of mitophagy-related proteins in mitochondrial fraction of differentiated adipocytes of WT and *Trx2^{ADKO}* mice at day 4 of differentiation. Inner membrane protein TOMM20 was used as a control. **(F)** Immunoblot analysis of NF-κB signaling proteins from differentiated adipocytes (day 4) of WT and *Trx2^{ADKO}* mice in the absence or presence of mito-TEMPO. **(G)** Representative immunoblot analysis of mitochondrial dynamics and mitophagy-related proteins from day differentiated adipocytes of WT and *Trx2^{ADKO}* mice in the absence or

presence of mito-TEMPO. **(H)** Representative immunoblot of NF- κ B signaling proteins and mitophagy-related proteins with and without IKK inhibitor BMS-345541 in differentiated adipocytes (day 4) of WT and *Trx2^{ADKO}* mice. Protein levels (C–H) were quantified and presented as fold changes by taking untreated WT as 1.0. $n = 3$ mice for each group. **(I)** Coimmunoprecipitation (IP) was performed using anti-IgG or anti-p62 and immunoblotting (IB) with anti-ubiquitin antibody (Ub) in differentiated adipocytes of WT and *Trx2^{ADKO}* mice at day 4. The experiment was repeated three times. **(J)** Confocal fluorescence images showing colocalization of p62 (green) and polyubiquitin (poly-Ub, purple) with mitochondria (TOMM20, red) in adipocytes of WT and *Trx2^{ADKO}* mice during differentiation. Images are representative of three independent experiments. Scale bars, 10 μ m. Quantitative data represent the mean \pm SEM. ***, $P < 0.001$ versus WT (two-tailed Student's t test).

mito-TEMPO abrogated both NF- κ B activation and p62-mediated mitophagy in *Trx2^{ADKO}* adipocytes (Fig. 6, F and G). BMS-345541, a small molecule inhibitor of IKK, abrogated the IKK-NF- κ B activation in *Trx2*-KO adipocytes. Furthermore, we observed that p62, LC3-II, and Beclin-1 expression was attenuated in *Trx2^{ADKO}* adipocytes by BMS-345541 (Fig. 6 H), indicating that p62-mediated mitophagy induced by *Trx2* deletion is NF- κ B dependent.

The p62 protein, which serves as a multifunctional signaling scaffold as well as an adaptor, binds polyubiquitinated proteins and damaged mitochondria and targets them to autophagosomes via its ubiquitin-associated domain and LC3-binding motif, respectively (Matsumoto et al., 2011). We therefore asked whether *Trx2* KO induces p62 to bind damaged mitochondria via its ubiquitin association domain. Coimmunoprecipitation of p62 followed by Western blotting with ubiquitin demonstrated a greater interaction between p62 and ubiquitinated proteins in *Trx2^{ADKO}* adipocytes than that in controls (Fig. 6 I). Furthermore, confocal fluorescence images showed that p62 was colocalized with K63-linked polyubiquitinated protein aggregates anchoring to the mitochondria in *Trx2^{ADKO}* adipocytes on days 4–12 upon *Trx2* deletion; the colocalization of p62/polyubiquitin with mitochondrial marker TOMM20 was not detected in control adipocytes (Fig. 6 J). Taken together, these data suggest that *Trx2* deficiency results in NF- κ B-dependent p62 accumulation and recruitment to the polyubiquitinated mitochondria, promoting mitophagy.

Elevated oxidative stress–NF- κ B–p62 pathway in adipose tissues from T2DM patients

To determine the clinical significance of the *Trx2*–NF- κ B–p62 pathway, we first analyzed available RNA-sequencing datasets from lean, obese, and T2DM patients. A heatmap analysis showed the top 100 up-regulated and down-regulated genes from lean, obesity, and T2DM groups, indicating alteration of the transcriptome landscape in human adipocytes (Fig. 7 A). There were comparative number of differential expressions of genes in the obesity (153 up-regulated and 76 down-regulated genes) and T2DM (188 up-regulated and 160 down-regulated genes) groups compared with the lean group, respectively (Fig. 7, B and C). Interestingly, a Kyoto Encyclopedia of Genes and Genomes (KEGG) pathway enrichment analysis of differentially expressed genes (DEGs) revealed that the ROS pathway, NF- κ B signaling, and fatty acid metabolism were altered in T2DM adipocytes (Fig. 7 D). Concomitantly, we confirmed the expression of key genes related to ROS regulation, inflammation, and fatty acid metabolism, including *TRX2*, glutathione Prx3, TNF- α , IL-6, FASN, and fatty acid-binding protein 2. The expression of cellular antioxidant genes (*TRX2* and glutathione Prx3) and fatty acid metabolism-related genes

(FASN and fatty acid-binding protein 2) were significantly suppressed in adipocytes of T2DM patients, whereas inflammation-related genes (TNF- α and IL-6) were markedly increased compared with the lean group (Fig. 7 E). Together, our results indicate that oxidative stress and NF- κ B signaling are implicated in the development and progression of T2DM.

To identify the gene expression signature of inflammation, gene set enrichment analysis (GSEA) indicated that most of the DEGs were involved in NF- κ B signaling in adipocytes of T2DM (Fig. 7, F and G). To further investigate the association of the *Trx2*–NF- κ B signaling with T2DM and concomitant hepatic steatosis in humans, we assessed *Trx2* expression in visceral WAT biopsies from nondiabetic (ND) subjects and patients with T2DM concomitant with hepatic steatosis (T2DM-HS; Table S1). Visceral adipose tissue biopsies from patients with T2DM-HS were obtained during laparoscopic inguinal hernia repair and laparoscopic cholecystectomy. T2DM-HS patients had lower levels of *Trx2* mRNA but augmented TNF- α mRNA levels in the visceral WAT compared with ND controls by real-time PCR (Fig. 7, H and I). T2DM-HS patients showed reduced *Trx2* and increased levels of phospho-P65/RelA, and elevated P65 was in the nucleus of adipocytes (Fig. 7, J and K). These results indicate that reduced *Trx2* expression and increased NF- κ B activation are implicated in T2DM-HS disease in humans. Additionally, gene expression of *Pink1*, *PRKN*, and *SQSTM1* was markedly increased in the visceral WAT of T2DM-HS patients compared with ND controls (Fig. 7, L–N), suggesting augmented mitophagy in the visceral fat of T2DM-HS patients.

Taken together, our data indicate a clinical association of the *Trx2*–NF- κ B–p62 pathway with human T2DM and T2DM-HS.

ROS scavenger and NF- κ B inhibitor ameliorates adipose mitophagy and hepatic insulin resistance-related T2DM

We reasoned that blockade of mitochondrial ROS or NF- κ B could have rescue effects on adipose metabolic dysfunction and T2DM phenotype in the *Trx2^{ADKO}* mouse model. To this end, WT and *Trx2^{ADKO}* mice at the age of 6 wk received a daily injection of mito-TEMPO (0.7 mg/kg/d by i.p. injection) or saline for 8 wk. Mito-TEMPO significantly attenuated weight loss and blood glucose elevation in *Trx2^{ADKO}* mice without any effects on WT mice (Fig. S5, A and B). Accordingly, mito-TEMPO normalized eWAT morphology and adipocyte size in *Trx2^{ADKO}* mice (Fig. S4 C). Mito-TEMPO attenuated mitochondrial ROS by 65% (Fig. S5 D) and reduced NF- κ B activation (phosphor-p65) by 60% in *Trx2^{ADKO}* eWAT that was induced by *Trx2* deletion, as indicated by Western blotting (Fig. S5 E) and by coimmunostaining of phospho-p65 with FABP4 (Fig. S5, F and G). Correlated with attenuated NF- κ B signaling, mito-TEMPO decreased mitophagy markers p62 and LC3II, decreased HSL protein but increased

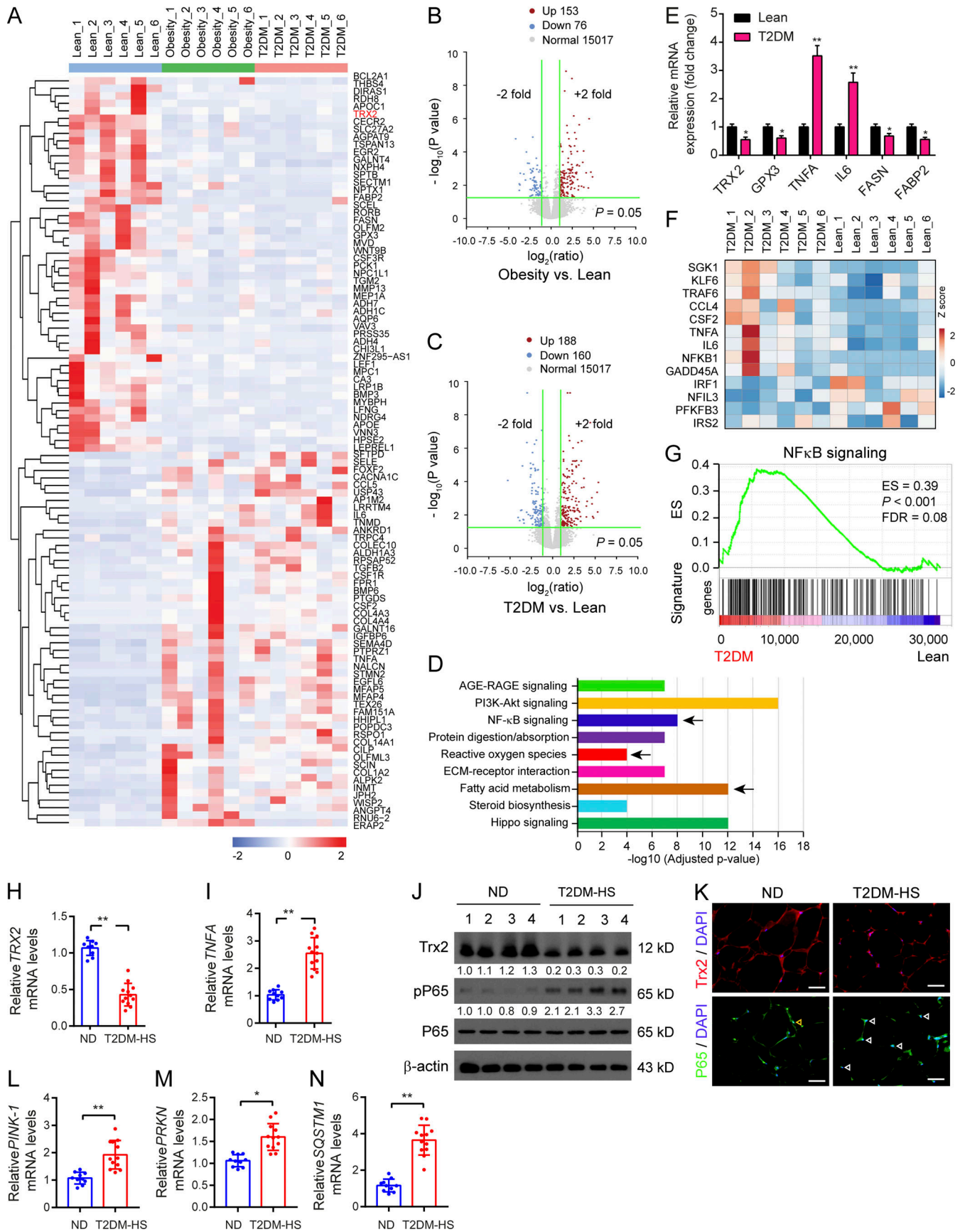


Figure 7. **Elevated oxidative stress–NF- κ B–p62 pathway in adipose tissues from T2DM patients.** (A) The heatmap displayed DEGs among isolated primary human adipocytes from the lean, obesity, and T2DM groups using hierarchical clustering analysis ($n = 6/\text{group}$). (B and C) Statistical analysis of RNA-sequencing gene expression for obesity (B) and T2DM (C) compared with lean as volcano plots. (D) KEGG pathway analysis of DEGs indicated that ROS pathway, NF- κ B signaling, and fatty acid metabolism were affected pathway in T2DM adipocytes (arrow). (E) The mRNA level of representative genes related to ROS regulation, inflammation, and fatty acid metabolism in adipocytes ($n = 6/\text{group}$). (F) Heatmap showing the expression of key inflammatory activation related genes in adipocytes between the lean and T2DM groups. (G) GSEA demonstrating enrichment score (ES) of gene sets in RNA-sequencing data of adipocytes. Genes in each gene set were ranked by signal-to-noise ratio according to their differential expression between the lean group and the T2DM group. FDR, false discovery rate. (H–N) Trx2–NF- κ B analyses in ND subjects ($n = 10$) and patients with T2DM-HS ($n = 12$). (H and I) Relative levels of *Trx2* and *TNFA* mRNA in visceral adipose tissues. (J) Representative Western blot analysis of Trx2, phospho-P65, and P65 in individual visceral adipose tissues of ND and T2DM-HS. Protein levels were quantified and presented as fold changes by taking WT as 1.0. $n = 4$ for each group. (K) Representative immunofluorescence staining of Trx2 and P65 in visceral adipose tissues from ND and T2DM-HS. (L–N) Gene expression of *PINK-1*, *PRKN*, and *SQSTM1* in isolated visceral adipose tissues from ND and T2DM-HS patients. Quantitative data are presented as mean \pm SEM. ns, not significant, *, $P < 0.05$; **, $P < 0.01$ versus corresponding control. Significance was assessed by two-tailed Student's *t* test. Scale bars, 50 μm (K). AGE-RAGE, advanced glycation end product–receptor for advanced glycation end product.

Glut4 expression (Fig. S5 E) with increased ATP content (Fig. S5 H) in *Trx2^{ADKO}* eWAT, suggesting improved glucose and lipid metabolism in *Trx2^{ADKO}* mice by mito-TEMPO. Similarly, serum levels of NEFA, adiponectin, and TG (Fig. S5, H–J) were partially rescued by mito-TEMPO. Much higher doses (10–30 mg/kg/d) have been used for acute injury models, such as sepsis, for a short period (<24 h; Patil et al., 2014). We chose a lower dose in our chronic treatment, explaining the partial rescue effects on the *Trx2^{ADKO}* D2M phenotype.

One well-characterized compound is BMS-345541, which inhibits both IKK2 (half-maximal inhibitory concentration = 0.3 μM) and IKK1 (half-maximal inhibitory concentration = 4 μM), but not a panel of 15 other cellular protein kinases (Herrmann et al., 2005). To directly examine the contribution of NF- κ B activation to the phenotype of *Trx2^{ADKO}* mice, 6-wk-old male *Trx2^{ADKO}* mice received BMS-345541 (60 mg/kg by i.p. injection) for 8 wk. BMS-345541 significantly attenuated body weight loss and blood glucose elevation (Fig. 8, A and B). Histology analysis showed that BMS-345541 eliminated hepatic lipid accumulation (Fig. 8 C), which consisted of a reduction in toxic lipids characterized by lower hepatic and serum triacylglycerol content in *Trx2^{ADKO}* mice (Fig. 8, D and E). Importantly, BMS-345541 treatment affirmatively inhibited NF- κ B activation and mitophagy, as demonstrated by the reduction of phospho-P65/RelA, p62, and LC3-II levels in eWAT of *Trx2^{ADKO}* mice (Fig. 8 F). Moreover, TEM results showed an alleviation of adipose mitochondrial damage in *Trx2^{ADKO}* mice after BMS-345541 treatment, which was reflected by an increase in the number of mitochondria and cristae surface area but a lower percentage of damaged mitochondria without detectable mitophagy (Fig. 8 G). Increased Glut4 levels and decreased HSL protein expression suggested improvements in glucose and lipid metabolism in *Trx2^{ADKO}* mice by BMS-345541 treatment (Fig. 8 F). Moreover, treating *Trx2^{ADKO}* mice with BMS-345541 normalized serum TNF- α , IL-6, and mitochondrial ATP, serum NEFA, adiponectin, and leptin to levels closer to those of controls (Fig. 8, H–L). Consequently, these results support a critical role of adipose mitochondrial ROS–NF- κ B signaling in the induction of adipose mitophagy and hepatic insulin resistance–related T2DM.

Discussion

Adipose tissue disorders cause alterations to adipose distribution and adipose dysfunction, with broad effects on

glucose and lipid metabolism and on secretion of cytokines, chemokines, and adipokines (Hajer et al., 2008; Moon et al., 2013; Shulman, 2014). The changes appear to induce chronic systemic inflammation and reduce insulin sensitivity, suggesting that recovery of WAT function may be an effective therapeutic approach for treating these disorders. Despite intense interest, the molecular mechanisms contributing to disturbed WAT activity that occur with hepatic insulin resistance–related T2DM are not fully understood.

In the present study, we offer a detailed analysis of a new transgenic mouse model with mitochondrial loss and dysfunction that demonstrates a strong relationship between adipose dysfunction and whole-body metabolic abnormalities. We found that deletion of *Trx2* in adipocytes exacerbates the development of hyperglycemia, whole-body and hepatic insulin resistance, and hepatic steatosis. Our study confirmed that loss of adipocyte *Trx2* leads to defects in mitochondrial structure and function, which suppress lipogenic genes but promote lipolytic gene expression in adipocytes, and finally results in abnormal energy metabolism. This not only increased plasma NEFA and glycerol concentrations, which in turn led to increased hepatic gluconeogenesis via the glycerol–dihydroxyacetonephosphate and the NEFA–acetyl-CoA–pyruvate carboxylase pathways (Perry et al., 2015), but also increased hepatic lipid accumulation and hepatic insulin resistance (Petersen and Shulman, 2018; Fig. 8 M). The effects of *Trx2* deficiency are induced by excessive ROS production, which disrupts mitochondrial dynamics and activates NF- κ B signal. Subsequently, NF- κ B activation promotes p62/SQSTM1 accumulation to recruit damaged mitochondria with polyubiquitin chains and thereby induces excessive mitophagy (Fig. 8 M). Importantly, NF- κ B inhibitors prevented NF- κ B/p62-mediated mitophagy and improved glucose and lipid metabolism, further ameliorated hepatic insulin resistance–related T2DM. Our data support that adipose mitophagy links WAT inflammation activation to hepatic insulin resistance and is consistent with prior observations (Perry et al., 2015).

Trx2 is a mitochondrial antioxidant that preserves mitochondrial integrity and function by protecting against excessive mitochondrial ROS (Huang et al., 2015). Mitochondria are the dominant source of ROS generation. The major site of endogenous mitochondrial ROS production during normal homeostasis is the mitochondrial electron transport chain, which is a component

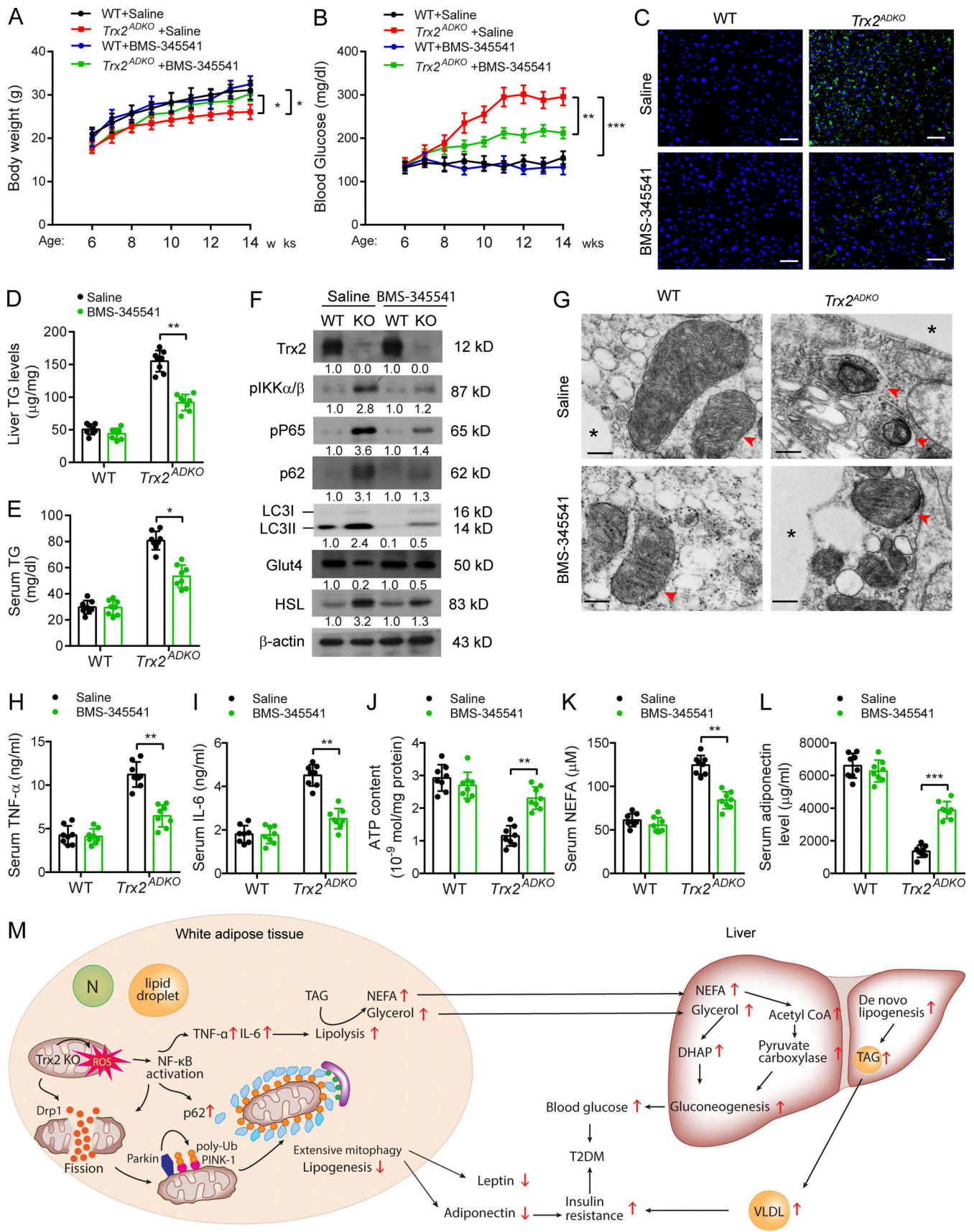


Figure 8. **Inhibition of NF-κB activity ameliorates T2DM in *Trx2*^{ADKO} mice.** 6-wk-old male *Trx2*^{ADKO} and WT mice were treated with 60 mg/kg BMS-345541 by i.p. injection once every 2 d for 8 wk. **(A and B)** Body weight (A) and fasting blood glucose levels (B) in WT and *Trx2*^{ADKO} mice with or without BMS-345541

treatment ($n = 8$) at the indicated ages. **(C)** Representative images of BODIPY staining showing liver lipid deposition of mice at 14 wk of age. Scale bars, 50 μm . **(D and E)** Liver TG content and serum TG level were measured. $n = 6$. **(F)** Immunoblot analysis of eWAT tissues from mice at 14 wk of age. Protein levels were quantified and presented as fold changes by taking WT as 1.0. $n = 3$ mice for each group. **(G)** Representative transmission electron micrographs of eWAT sections from mice at 14 wk of age (six images/mouse, $n = 3$ mice/group). Asterisks indicate LDs. Arrowheads indicate mitochondria. Scale bars, 0.5 μm . **(H and I)** Serum cytokines TNF- α and IL-6 proteins were measured by ELISA kits ($n = 8$). **(J)** ATP content of mitochondria isolated from eWAT of mice at 14 wk of age ($n = 8$). **(K and L)** Serum levels of NEFA (K) and adiponectin (L) of 14-wk-old mice ($n = 8$). Quantitative data are presented as mean \pm SEM. *, $P < 0.05$; **, $P < 0.01$; ***, $P < 0.001$ versus the indicated comparisons. Significance was assessed by one-way ANOVA followed by Tukey's post hoc test. **(M)** A schematic diagram summarizing our findings that Trx2 deficiency promotes severe mitophagy via mitochondrial ROS/NF- κB /p62 signaling, which contributes to hepatic insulin resistance related T2DM (see text for details). N, nucleus; DHAP, dihydroxyacetonephosphate. TAG, triacylglycerol; VLDL, very low-density lipoprotein.

of OXPHOS responsible for energy production (Chen et al., 2003). Dysregulation of electron transport chain function is present in many insulin-resistant states, including type 2 diabetes and obesity (Keller and Attie, 2010). In humans, down-regulation of OXPHOS genes (Patti et al., 2003) and decreased muscle mitochondria activity in skeletal muscle are associated with increased ectopic lipid content and muscle insulin resistance. We found that Trx2 deletion in adipocytes results in noticeably increased ROS generation and thus decreased OXPHOS complex I, II, III, and IV expression and ATP production, which may contribute to insulin resistance of adipose tissue.

Our study indicates that NF- κB signaling is the key effector for Trx2 in adipocytes. It has been shown that Trx1 can directly enhance the DNA binding of NF- κB by reduction of a disulfide bond (Matthews et al., 1992). It is unclear if mitochondrial Trx2 has such an effect on NF- κB . Studies has revealed excessive ROS also induces the activation of the IKK, which in turn phosphorylates I κB , leading to NF- κB signaling activation (Formentini et al., 2012; Janssen-Heininger et al., 2000). Consistent with the effect of increased ROS generation on inflammation activation, we demonstrated deletion of Trx2 resulted in increased phosphorylation of IKK, I $\kappa\text{B}\alpha$, and NF- κB subunit p65/RelA, which activated NF- κB signaling in WAT and elevated TNF- α and IL-6 concentration in both WAT and serum. Besides increased inflammation in Trx2-deficient adipocytes, we demonstrate an important mechanism that NF- κB signaling is required for p62 recruitment and thus for inducing mitophagy in adipocytes. Specifically, the accumulated p62 binds damaged mitochondria via polyubiquitinated proteins and targets them for autophagosomal clearance. Interestingly, NF- κB , through p62-mediated removal of damaged mitochondria, could also restrain its own proinflammatory activity in macrophages, specifically by decreasing NLRP3 inflammasome activation (Zhong et al., 2016). In addition, ROS, thioredoxin-interacting protein (TXNIP), and NLRP3 inflammasome are all implicated in the inflammatory pathogenesis of T2DM (Schroder et al., 2010). TXNIP is a regulator of metabolism and an inhibitor of the antioxidant Trxes, including cytosolic Trx1 and mitochondrial Trx2 (Yoshioka et al., 2012). When intracellular O_2^- increases, NLRP3 dissociates from TXNIP and then binds to ASC (apoptosis-associated speck-like protein containing a CARD) and forms the NLRP3 inflammasome (Schroder et al., 2010). However, our data show that Trx2 deficiency in adipocytes results in NF- κB -dependent p62 accumulation to promote excessive mitophagy without effects on NLRP3-inflammasome activation (data not shown).

NF- κB signal activation initiates the inflammatory cascade in adipose tissue and is believed to orchestrate T2DM progression (Baker et al., 2011; Cai et al., 2005; Donath and Shoelson, 2011; Kiechl et al., 2013; Kondegowda et al., 2015). Our previous study showed that adipocyte-specific *Senp1* deletion induces NF- κB -dependent proinflammatory cytokine production in pancreatic adipose tissue (Shao et al., 2015). The resulting activation of immune cells, especially CD8 $^+$ and CD4 $^+$ T cells, leads to pancreatic islet β cell damage and T2DM progression (Shao et al., 2015). Moreover, recent studies have established that TNF- α affects adipocytes profoundly and results in the attenuation of insulin signaling and inhibition of adipogenesis. IL-6 infusion causes hepatic insulin resistance in rodents, in part by promoting adipose tissue lipolysis (Perry et al., 2015). Collectively, results of the present study suggest that NF- κB signal activation induced by mitochondrial ROS contributes to adipose dysfunction and thus hepatic insulin resistance-related T2DM progression in *Trx2^{ADKO}* mice. This conclusion is supported by the following evidence: (1) NF- κB -dependent p62/SQSTM1 accumulation induces excessive mitophagy, disrupting glucose and lipid metabolism in adipocytes; (2) elevated levels of the inflammatory cytokines TNF- α and IL-6 disrupt lipogenesis and lipolysis in adipocytes, contributing to hepatic steatosis and hepatic insulin resistance; and (3) abnormally low circulating levels of adiponectin and leptin lead to whole-body insulin resistance, contributing to T2DM progression.

Mitochondria are vital for maintaining metabolic homeostasis in white adipocytes, through regulating of adipogenesis, lipolysis, fatty acid synthesis and esterification, and branched-chain amino acid catabolism (Wilson-Fritch et al., 2004). Indeed, mitochondrial components and oxidative capacity are essential for white adipose metabolism (Patti and Corvera, 2010; Wilson-Fritch et al., 2004). Several studies have reported the potential role of adipose mitochondrial dysfunction in metabolic abnormalities. Adipocyte-specific deletion of the gene encoding mitochondrial transcription factor A (*Tfam*) decreased OXPHOS enzyme activity and promoted cell death and inflammation. The *Tfam* KO mice were resistant to weight gain (Vernochet et al., 2012) and exhibited insulin resistance, hepatosteatosis, and cardiovascular complications (Vernochet et al., 2014). Inactivation of autophagy by *Atg7* deletion in adipose tissue at early stages of development increased mitochondrial content and adipogenesis, increasing insulin sensitivity (Zhang et al., 2009). However, blocking autophagy in mature adipose tissue caused accumulation of dysfunctional mitochondria and induced peripheral insulin resistance (Cai et al., 2018). Therefore,

autophagy/mitophagy may play different roles in various stages of adipose tissues. The direct contribution of mitophagy to the T2DM phenotype in *Trx2*-deficient mice needs further investigation. The clinical significance of our current work is that our transcriptome analyses in human adipocytes, based on available RNA-sequencing datasets from lean, obese, and T2DM patients, reveal that the mitochondrial pathway and NF- κ B signaling are altered in T2DM adipocytes. Moreover, we observed a considerable reduction of *Trx2* expression in visceral WAT of T2DM-HS patients, concomitant with a significant NF- κ B signal activation. Importantly, NF- κ B inhibitors substantially reversed hepatic insulin resistance-related T2DM through improving systemic glucose and lipid metabolism in *Trx2^{ADKO}* mice. These findings suggest the potentiality of blocking inflammation activation in the treatment of hepatic insulin resistance and T2DM associated with adipose mitophagy.

In summary, our experiments demonstrated a strong relationship between adipose mitochondrial function and systemic metabolism. Excessive mitophagy in adipose tissue links NF- κ B signal activation to hepatic insulin resistance and type 2 diabetes, which can disturb whole-body metabolic homeostasis. This study has provided a molecular mechanism for the pathogenesis of hepatic insulin resistance-related T2DM and may help to develop a novel therapeutic strategy for the treatment of diabetes.

Materials and methods

Animals

To generate mice with adipocyte-specific deletion of *Trx2*, *Trx2^{+lox}* mice were generated by inserting loxP sites flanking *Trx2* gene exon 3 by homologous recombination, as described previously (Huang et al., 2015). *Trx2^{lox/lox}* mice were generated by intercrossing *Trx2^{+lox}* mice. The *Trx2^{lox/lox}* mice were then crossed to transgenic mice expressing Cre recombinase driven by the adiponectin gene promoter (The Jackson Laboratory; stock 028020) to obtain *Trx2^{ADKO}* (*Trx2^{lox/lox};Adipo-Cre*). All mice were backcrossed with C57BL/6 mice for >10 generations. KO of *Trx2* in adipocytes was verified by real-time PCR with primers amplifying *Trx2* exon 3 (Huang et al., 2015), and adipocyte-specific Cre (Shao et al., 2015). *Trx2^{lox/lox}* mice were used as WT controls. Male and female animals were used in equal numbers for baseline experiments, and both males and females exhibited similar phenotype in blood glucose levels and adipose tissues. We used males only for further experiments, and littermates were compared in all studies. The mice were maintained on a 12-h/12-h light/dark cycle (lights on at 7 a.m.) with unlimited access to food and water. For HFD experiments, 6-wk-old mice were fed with either the NCD or an HFD containing 45% kcal fat, 35% kcal carbohydrate, and 20% kcal protein (Research Diets; D12108C) for 8 wk. All animal procedures conformed to National Institutes of Health guidelines and were approved by the Yale University Animal Care and Use Committee.

Evaluation of metabolic phenotype in *Trx2^{ADKO}* mice

Mice were fasted overnight before metabolic analysis, and blood samples were drawn from the retro-orbital plexus of the fasting

mice under anesthesia. We used ELISAs to determine serum levels of insulin (ALPCO; 80-INSMSU-E01), leptin (ALPCO; 22-LEPMS-E01), and adiponectin (R&D Systems; MRP300). We used a colorimetric/fluorometric kit to determine serum and tissue levels of NEFAs (BioVision; K612) and ELISA kits to determine serum and tissue levels of TNF- α (R&D Systems; SMTA00B) and IL-6 (R&D Systems; SM6000B and S6050). We measured serum cholesterol and TG levels with a Cobas Mira analyzer (Roche Diagnostics) at the Mouse Metabolic Phenotyping Center in Yale University.

For glucose tolerance tests (GTTs), we determined basal fasting glucose levels and then administered dextrose (1 g/kg body weight) by i.p. injection. For ITTs, we administered insulin (0.35 U/kg body weight for NCD-fed mice, 0.6 U/kg body weight for HFD-fed mice) by i.p. injection. We obtained blood samples from the tail vein 15, 30, 60, and 120 min after injection and determined blood glucose levels using a glucometer (LifeScan).

Indirect calorimetry

We measured food intake, water consumption, oxygen consumption (VO_2), carbon dioxide production (VCO_2), and energy expenditure in 14-wk-old male *Trx2^{ADKO}* mice and WT littermates ($n = 6$ per group) using a comprehensive laboratory animal metabolic system (Columbus Instruments) at the Yale Mouse Metabolic Phenotyping Center. The RER was calculated as VCO_2/VO_2 .

Hyperinsulinemic-euglycemic clamp study

Basal infusion and hyperinsulinemic-euglycemic clamp studies were used to assess whole-body and hepatic insulin sensitivity as previously described (Perry et al., 2015). After surgical implantation of an indwelling catheter in the right jugular vein and advanced to the right atrium of the heart, the mice ($n = 10$ per group) were allowed to recover for 1 wk before clamp experiments. In short, a continuous infusion of regular insulin and [$3\text{-}^3\text{H}$] glucose was administered at 7.14 mU/(kg·min) and 0.24 Ci/min, respectively, for 4 min, after which the rates were reduced to 3 mU/(kg·min) insulin and 0.1Ci/min [$3\text{-}^3\text{H}$] glucose for the remainder of the experiment. Blood was collected via tail massage for plasma glucose, insulin, and tracer levels at set time points 10–20 min apart throughout the 140-min infusion, and a variable infusion of 20% dextrose was given to maintain euglycemia. Hepatic glucose production represents the difference between the rate of glucose appearance and the glucose infusion rate. Whole-body glucose uptake was calculated as previously described (Kim et al., 2000). Plasma NEFA concentrations were measured using a Wako reagent (Wako Diagnostics).

Isolation of adipose tissue depots

Adipose tissues were divided into WAT and BAT based on visual impression, and WAT depots were further divided into subcutaneous WAT and visceral WAT. IngWAT is anterior to the upper segment of the hindlimbs, which is the largest subcutaneous WAT depot in mice. Other subcutaneous WATs include interscapular WAT, axillary WAT, and vertebral WAT. eWAT is the largest the largest visceral WAT depot in mice. To avoid contamination by the vas deferens, testicular arteries, and epididymis, we

collected only the top portion of eWAT. Other visceral WATs, including perirenal WAT and mesenteric WAT, were also evaluated in our study.

We used interscapular BAT because it is the largest BAT depot in mice located above the shoulder blades. The overlying subcutaneous WAT was carefully removed during isolation of the interscapular BAT.

Histology and immunofluorescence

Formalin-fixed paraffin-embedded tissues were cut into 5- μ m-thick sections. Hematoxylin and eosin staining were conducted following standard protocols, and the stained tissue sections were visualized under a light microscope equipped a Kodak digital camera. Adipocyte size was determined using ImageJ software (NIH).

Immunofluorescence analysis was performed as previously described (Zhou et al., 2016) using primary antibodies against the following proteins and peptides: Trx2 (Santa Cruz; catalog no. sc-50336), FABP4 (Cell Signaling Technology; catalog no. 3544; and Abcam; catalog no. ab93945), p62/SQSTM1 (Cell Signaling Technology; catalog no. 7695), phospho-NF- κ B p65 (Cell Signaling Technology; catalog no. 3033), NF- κ B p65 (Cell Signaling Technology; catalog no. 8242), F4/80 (BioLegend; catalog no. 123116), TOMM20 (Abcam; catalog no. ab56783), insulin (Cell Signaling Technology; catalog no. 8138), and glucagon (Abcam; catalog no. ab10988). TUNEL (Roche; catalog no. 11684795910) staining performed according to the manufacturer's instructions. Fluorescent images were acquired using a fluorescence microscope (Zeiss).

Immunofluorescent staining

Preadipocytes and adipocytes were assessed by immunofluorescent staining during differentiation (on days 0, 4, 8, and 12). Cells cultured in 35-mm glass-bottom culture dishes were washed with PBS and then fixed with 2% paraformaldehyde at room temperature for 20 min. The cells were then permeabilized with 0.1% Triton X-100 and blocked in 1% BSA with 1% donkey serum for 60 min. After overnight incubation at 4°C with the primary antibodies p62/SQSTM1 (Cell Signaling Technology; catalog no. 7695), TOMM20 (Abcam; catalog no. ab56783), and K63 linkage-specific ubiquitin Alexa Fluor 647 (Abcam; catalog no. ab192489), the cells were incubated with secondary fluorescent antibodies and counterstained with Vectashield mounting medium with DAPI (Vector Laboratories). Fluorescence images were obtained with an LSM 710 Duo confocal microscope (Zeiss).

LD staining

To assess ectopic lipid accumulation in the liver and quadriceps muscle we used the lipophilic dye BODIPY 493/503 (Molecular Probes). The 5- μ m-thick cryostat sections were washed with PBS, stained with 1 μ g/ml BODIPY at room temperature for 15 min, and then mounted with DAPI. At least three discontinuous areas of three sections were assessed for each group. Images were acquired using a fluorescence microscope (Zeiss).

We also used BODIPY to evaluate the differentiation efficiency of cultured adipocytes. Live cells (without fixation) were

stained with 1 μ g/ml BODIPY and counterstained with DAPI. We counted the number of LDs per cell ($n = 20$ cells per group) under a confocal microscope (Zeiss).

Immunoprecipitation

Immunoprecipitation was performed with differentiated adipocytes (day 8), according to the standard protocol. In brief, the cells were lysed with RIPA buffer on ice for 30 min with gentle shaking, followed by centrifugation at 12,000 $\times g$ at 4°C for 12 min. The whole-cell lysate (supernatant) was then transferred to a new 1.5-ml tube. For the input sample, 20 μ l whole-cell lysate was prepared with Laemmli buffer and boiled at 100°C for 5 min. For immunoprecipitation, the cell lysates were pre-cleared for 1 h with normal rabbit IgG (Cell Signaling Technology; catalog no. 3423) and protein A/G agarose beads (Santa Cruz; catalog no. sc-2003) that had been prewashed with RIPA buffer. After the beads were removed, the pre-cleared lysates were incubated overnight with 10 μ l p62/SQSTM1 (Cell Signaling Technology; catalog no. 5114) or control rabbit IgG at 4°C with rotation. Subsequently, agarose beads were added to the lysates, incubated for another 4 h, and then collected and washed with ice-cold RIPA buffer. Immunoprecipitates were eluted from the beads by boiling in Laemmli buffer. The supernatant was loaded on a 15% SDS-PAGE gel and probed with K63 linkage-specific polyubiquitin (Cell Signaling Technology; catalog no. 5621) according to the immunoblotting protocol.

Mitochondrial function in adipocytes

Cellular oxygen consumption of differentiated adipocytes was assessed using the Seahorse XF96 analyzer. Briefly, 20,000 preadipocytes isolated from eWAT were seeded into each well of gelatin-coated XF96 cell culture microplates and cultured in growth medium. 2 d after reaching confluence, the cells were differentiated in adipogenic medium for 2 d, after which they were cultured in maintenance medium for 8 d. On the day of experiment, the differentiated adipocytes were washed and then cultured in Agilent Seahorse XF Base Medium (supplemented with 25 mM glucose and 1 mM pyruvate) in a non-CO₂ incubator at 37°C for 1 h. The cells were then transferred to a temperature-controlled Seahorse analyzer to perform the mitochondrial stress test. After obtaining three basal respiration measurements, we obtained three respiration measurements after adding the coupled respiration inhibitor oligomycin (1 μ M) to assess ATP production and proton leak. We measured maximal respiration three times after adding 1 μ M carbonyl cyanide-4-(trifluoromethoxy) phenylhydrazone and measured spare respiratory capacity and nonmitochondrial respiration after adding 0.5 μ M rotenone and 0.5 μ M antimycin A. Results were analyzed with Wave software (Agilent Technologies).

Detection of mitochondrial ROS production and mitochondrial membrane potential

To measure mitochondrial ROS production in WAT samples, eWAT was isolated from 14-wk-old WT/Trx2^{ADKO} mice, placed in optimal cutting temperature compound (without fixation), and frozen. The fresh frozen 30- μ m sections were washed in PBS for 15 min and then incubated with 2.5 μ M mitoSOX (Molecular

Probes; M36008) at 37°C for 10 min followed by detection under microscope with the emission/excitation at 580/510 nm. The sections were washed again with PBS, stained with DAPI, and visualized using a fluorescent microscope (Zeiss). Fluorescence intensity were quantified in an average of six random fields per section. To determine mitochondrial ROS production in differentiated adipocytes (day 8), adherent cells were washed with PBS three times and then incubated in 2.5 μ M mitoSOX at 37°C for 10 min. Images were acquired using a confocal microscope (Zeiss).

To determine mitochondrial membrane potential, we used JC-1 (Molecular Probes; MP03168), a cationic dye that accumulates in mitochondria in a potential-dependent manner. When mitochondria lose membrane potential, fluorescence emission shifts from green (~525 nm) to red (~590 nm); thus, mitochondrial depolarization is indicated by a decrease in the red/green fluorescence intensity ratio. Adherent differentiated adipocytes (day 8) were washed with PBS and then loaded with 2.0 μ g/ml JC-1 at 37°C for 20 min in the absence of light. The cells were washed again, counterstained with DAPI, and viewed under a confocal microscope (Zeiss).

Clinical specimens

Human visceral adipose tissue was obtained from ND subjects ($n = 10$) and patients with T2DM-HS ($n = 12$). The ND subjects were recruited in the Department of Gastrointestinal Surgery, Guangzhou First People's Hospital. Exclusion criteria were malignancy, current inflammatory conditions, and chronic liver disease. Visceral adipose tissue biopsies from ND subjects were obtained during laparoscopic inguinal hernia repair. Patients who met the criteria of T2DM and concomitant hepatic steatosis (defined as the presence of definite hepatic steatosis on ultrasound scan of abdomen), were recruited in the Department of Gastrointestinal Surgery, Guangzhou First People's Hospital (Table S1). Visceral adipose tissue biopsies from patients with T2DM-HS were obtained during laparoscopic inguinal hernia repair and laparoscopic cholecystectomy. The study was approved by the Conjoint Health Research Ethics Board of Guangzhou First People's Hospital. Written informed consent was provided by all subjects before participation in this study.

Data source and bioinformatic analysis

Human adipocyte RNA-sequencing profiles of lean, obese, and T2DM patients ($n = 6$ each group) were downloaded from Gene Expression Omnibus database (<https://www.ncbi.nlm.nih.gov/geo/>). The series accession no. is GSE133099 and the matched-platform accession no. is GPL16791. Differentially expressed mRNAs among lean, obesity, and T2DM adipocytes were selected and visualized using R software (version 3.4.1, DESeq2 and pheatmap packages). In brief, data were processed for selecting out DEGs with screening criteria adjusted P value <0.05 and $|\text{fold change}| > 1$. In addition, GSEA software (<http://software.broadinstitute.org/gsea>) and the KEGG database (<https://www.genome.jp/kegg/>) were adopted to unveil significantly enriched signaling pathways.

Preadipocyte isolation and differentiation

Epididymal WAT from 8-wk-old male *Trx2^{lox/lox}*, Adipo-Cre and WT (*Trx2^{lox/lox}*) mice was isolated, weighed, and minced. Small

pieces of adipose tissue were digested in enzyme solution (Hank's buffered salt solution containing 4% fatty acid-free BSA, 2.5% penicillin/streptomycin, and 1 mg/ml collagenase type 2) at 37°C for 50 min with gentle shaking. After filtering through a 100- μ m filter to remove undigested tissue, the cell suspension was centrifuged for 10 min at 1,200 rpm. The cell pellet containing preadipocytes was then resuspended in growth medium (minimum essential medium, 10% fetal bovine serum, 1% penicillin/streptomycin, and 25 mM NaHCO₃) and plated onto a 10-cm cell culture dish. The medium was refreshed every 3 d. After reaching confluence, the cells were trypsinized and seeded onto 6-well cell culture plates in growth medium. After being held at confluence for 48 h without changing the medium, the cells were differentiated by incubation in adipogenic medium (growth medium supplemented with 0.25 μ M dexamethasone, 0.17 μ M insulin, and 135 μ M 8-methoxymethyl-3-isobutyl-1-methylxanthine) for 2 d. 2 d after the induction of differentiation (day 0), the cell culture medium was switched to maintenance medium (growth medium supplemented with 0.17 μ M insulin). At different time points during differentiation (day 0, 4, 8, or 12), Adipo-Cre was expressed in mature adipocytes from *Trx2^{lox/lox}* Adipo-Cre mice; therefore, the *Trx2* gene was specifically deleted in these cells, but not in mature adipocytes from WT (*Trx2^{lox/lox}*) mice. Cells were harvested for RNA and protein extraction, analyzed by immunofluorescence staining, or used to measure mitochondrial respiration.

TEM

TEM was performed by the Yale Biological Electron Microscopy facility. To process tissues for TEM, adipose, pancreatic, and kidney tissue was isolated from mice and immediately cut into small pieces (1 μ m \times 1 μ m \times 1 μ m) in ice-cold PBS. The tissue pieces were gently shaken with electron microscopy fixation buffer (2.5% glutaraldehyde and 2% paraformaldehyde in 0.1 M sodium cacodylate [pH 7.4]) at room temperature for 30 min and then incubated at 4°C for another 90 min. The tissue samples were washed three times with 0.1 M Na cacodylate buffer (pH 7.4).

To process cells for TEM, differentiated adipocytes (day 8) in 10-cm culture dishes were fixed in prewarmed 2.5% glutaraldehyde in 0.1 M sodium cacodylate (pH 7.4) at room temperature for 30 min and then incubated at 4°C for another 60 min. The cells were washed three times with 0.1 M sodium cacodylate buffer (pH 7.4).

Subsequent processing was performed by the Yale electron microscopy facility. Specimens were viewed on a FEI Tecnai BioTWIN transmission electron microscope at an accelerating voltage of 80 kV, and images were obtained with a SIS Morada 11-megapixel charge-coupled device camera and iTEM software (Olympus).

Real-time PCR analysis and mitochondrial DNA quantification

Total RNA was extracted from adipose tissue and cultured adipocytes with the RNeasy RNA Mini Kit (Invitrogen). cDNA was synthesized from 1 μ g total RNA using the iScript cDNA Synthesis Kit (Bio-Rad). Real-time PCR was performed on an iCycler Real-Time Detection System (Bio-Rad) with iQ SYBR Green

Supernatant (Bio-Rad) and gene-specific primers. Mitochondrial DNA was measured by real-time PCR as described previously (Huang et al., 2015). Target gene expression was normalized to *Actb* or 18S rRNA. Real-time PCR primers are listed in Table S2.

Adipose tissue protein extracts and Western blot analysis

Adipose tissues were carefully dissected and collected on dry ice. Tissues were minced by scissors and lysed in 2× Laemmli buffer with 300 μl/50 mg adipose tissue. Tissue lysates were boiled for 5 min at 100°C followed by centrifugation at 20,000× *g* for 15 min at 4°C. The top lipid layer was removed, and the middle layer with adipose protein extracts was collected without the bottom layer. The collected protein extracts were subjected to standard Western blot analysis, which was performed as previously described (Huang et al., 2015). To analyze OXPHOS, protein samples were warmed at 37°C instead of 100°C to avoid degradation of the heat-sensitive complexes. The following antibodies were used for Western blotting: Trx2 (Abcam; catalog no. ab185544), β-actin (Santa Cruz; catalog no. sc-47778), phospho-NF-κB p65 (Cell Signaling Technology; catalog no. 3033), NF-κB p65 (Cell Signaling Technology; catalog no. 8242), phospho-IKKα/β (Cell Signaling Technology; catalog no. 2697), IKKβ (Cell Signaling Technology; catalog no. 2370), phospho-IκBα (Cell Signaling Technology; catalog no. 2859), IκBα (Cell Signaling Technology; catalog no. 4814), phospho-AKT (Cell Signaling Technology; catalog no. 4060), AKT (Cell Signaling Technology; catalog no. 4691), mitofusin-1 (Abcam; catalog no. ab57602), OPA1 (Abcam; catalog no. ab42364), Fis1 (Enzo Life Science; catalog no. Alx-210-1037), Drp1 (Abcam; catalog no. ab56788), p62/SQSTM1 (Cell Signaling Technology; catalog no. 5114), NBR1 (Cell Signaling Technology; catalog no. 9891), LC3B (Cell Signaling Technology; catalog no. 2775), Beclin-1 (Santa Cruz; catalog no. sc-48341), CIT1 (Cell Signaling Technology; catalog no. 14309), IDH1 (Cell Signaling Technology; catalog no. 8137), OGDH (Cell Signaling Technology; catalog no. 26865), total OXPHOS Rodent WB Antibody Cocktail (Abcam; catalog no. ab110413), PRX3 (Abcam; catalog no. ab73349), Glut4 (Santa Cruz; catalog no. sc-53566), HSL (Cell Signaling Technology; catalog no. 4107), PPARγ (Santa Cruz; catalog no. sc-7273), Caspase-3 (Cell Signaling Technology; catalog no. 9665), voltage-dependent anion channel (Cell Signaling Technology; catalog no. 4661), ATG7 (Abcam; catalog no. ab133528), PINK1 (Abcam; catalog no. ab75487), and Parkin (Santa Cruz; catalog no. sc-136989).

Isolation of mitochondria and assessment of mitochondrial function

For adipose tissues, we collected mitochondria from freshly collected (not frozen) WAT using a mitochondria isolation kit for tissue (Thermo Scientific; 89801) according to the manufacturer's instructions. For differentiated adipocytes, we used a mitochondrial isolation kit for cultured cells (Thermo Scientific; 89874). The cytosolic fraction and pellet containing mitochondria were boiled with Laemmli buffer, loaded on an SDS-PAGE gel, and analyzed by Western blotting.

To determine the amount of ATP generated by the mitochondria, the cell pellet containing mitochondria was resuspended

in sterile distilled water and assessed with an ATP bioluminescent assay kit (Sigma-Aldrich; FLAA) following the manufacturer's protocol.

Antioxidant treatment and NF-κB signaling inhibition

On the day of differentiation induction, preadipocytes isolated from *Trx2^{ADKO}* and WT mice were treated with the mitochondria-targeted antioxidant mito-TEMPO (25 μM in normal saline; Enzo; ALX-430-150) or the IKK inhibitor BMS-345541 (10 μM; Sigma-Aldrich; B9935) in adipogenic medium. After 48 h, the cells were cultured in maintenance medium containing mito-TEMPO or BMS-345541. Control groups were treated with DMSO. On day 4, the cells were harvested for Western blotting analysis or immunofluorescent staining.

For in vivo experiments, WT and *Trx2^{ADKO}* mice at age 6 wk received injection of mito-TEMPO (0.7 mg/kg/d by i.p. injection once every 2 d) or vehicle (saline). For NF-κB signaling inhibition in vivo, 6-wk-old male *Trx2^{ADKO}* and WT mice were treated with 60 mg/kg BMS-345541 by i.p. injection once every 2 d for 8 wk. Controlled *Trx2^{ADKO}* and WT mice were injected with same volume of normal saline (each treatment group, *n* = 8). Body weight and blood glucose levels were measured weekly. At the age of 14 wk, the mice were killed for histological and molecular analyses.

Statistics

We performed all statistical analyses with SPSS 17.0 statistical software package. All quantitative data are presented as mean ± SEM. Two-group comparisons were performed using two-tailed Student's *t* test. Multigroup comparisons were performed using one-way ANOVA followed by Tukey's post hoc test. We did not use a statistical method to predetermine sample size. Sample distribution was evaluated by the Kolmogorov-Smirnov test. Nonnormal data were evaluated by Spearman's rank-order correlation test. *P* < 0.05 was considered significant.

Online supplemental material

Fig. S1 shows *Trx2* targeting strategy and adipocyte-specific deletion. Fig. S2 shows type 2 diabetic phenotype of adipocyte-specific *Trx2*-KO mice. Fig. S3 shows T2DM-related end-organ damage in pancreas, kidney, liver, and BAT. Fig. S4 shows *Trx2* deficiency increases ROS in isolated adipocytes and alters mitochondrial energetics and oxidative metabolism. Fig. S5 shows that mitochondria-specific antioxidant mito-TEMPO ameliorates adipocyte dysfunction and T2DM in *Trx2^{ADKO}* mice. Table S1 shows anthropometric and clinical variables of the study subjects. Table S2 shows primer sequences used for real-time PCR analysis.

Acknowledgments

We are grateful to X. Liu (Yale University School of Medicine) for assistance with the TEM study. We thank J. Cao (Guangzhou First People's Hospital, Guangzhou, China) for clinical specimens.

This work was partly supported by National Institutes of Health grants R01 HL109420, HL115148, R01 DK113984, R01 DK114793,

R01 DK116774, and P30 DK045735. H. Jenny Zhou is supported by an American Heart Association National Career Development Award (19CDA34760284).

Author contributions: F. He, Y. Huang, Z. Song, H. Jenny Zhou, G.I. Shulman, and W. Min conceived the study, designed experiments, and wrote the manuscript. F. He, Y. Huang, and Z. Song contributed all in vivo and in vitro experiments. H. Zhang and H. Jenny Zhou contributed to the generation of the gene KO mice. R.J. Perry and G.I. Shulman contributed the experiments for energy expenditure and hyperinsulinemic-euglycemic clamp. F. He, Y. Huang, R.J. Perry, G.I. Shulman, and W. Min interpreted the data. G.I. Shulman and W. Min supervised the entire project and edited the manuscript.

Disclosures: G. Shulman reported grants from NIH (R01 DK119668, R01 DK116774, R01 DK113984, R01 DK114793, RC2 DK120534, and P30 DK045735), Gilead Sciences, Inc., AstraZeneca, and Merck & Co., Inc.; non-financial support from Gilead Sciences, Inc., AstraZeneca, Merck & Co., Inc., Janssen Research & Development, and Novo Nordisk; and personal fees from Gilead Sciences, Inc., AstraZeneca, Merck & Co., Inc., Janssen Research & Development, Novo Nordisk, iMetabolic Biopharma Corp., Maze Therapeutics, Inc., Genierian Pharmaceuticals, Ionis Pharmaceuticals, Inc., BridgeBio, Esperion, 89Bio, Inc., Nimbus Discovery, Inc., Staten Biotechnology, Longitude Capital, Celgene Corp., and Aegerion Pharmaceuticals during the conduct of the study. No other disclosures were reported.

Submitted: 6 July 2020

Revised: 2 September 2020

Accepted: 19 October 2020

References

Baixauli, F., N.B. Martin-Cofreces, G. Morlino, Y.R. Carrasco, C. Calabialinares, E. Veiga, J.M. Serrador, and F. Sanchez-Madrid. 2011. The mitochondrial fission factor dynamin-related protein 1 modulates T-cell receptor signalling at the immune synapse. *EMBO J.* 30:1238-1250. <https://doi.org/10.1038/emboj.2011.25>

Baker, R.G., M.S. Hayden, and S. Ghosh. 2011. NF-kappaB, inflammation, and metabolic disease. *Cell Metab.* 13:11-22. <https://doi.org/10.1016/j.cmet.2012.12.008>

Bi, P., T. Shan, W. Liu, F. Yue, X. Yang, X.R. Liang, J. Wang, J. Li, N. Carlesso, X. Liu, and S. Kuang. 2014. Inhibition of Notch signaling promotes browning of white adipose tissue and ameliorates obesity. *Nat. Med.* 20: 911-918. <https://doi.org/10.1038/nm.3615>

Birkenfeld, A.L., and G.I. Shulman. 2014. Nonalcoholic fatty liver disease, hepatic insulin resistance, and type 2 diabetes. *Hepatology.* 59:713-723. <https://doi.org/10.1002/hep.26672>

Bogacka, I., H. Xie, G.A. Bray, and S.R. Smith. 2005. Pioglitazone induces mitochondrial biogenesis in human subcutaneous adipose tissue in vivo. *Diabetes.* 54:1392-1399. <https://doi.org/10.2337/diabetes.54.5.1392>

Cai, D., M. Yuan, D.F. Frantz, P.A. Melendez, L. Hansen, J. Lee, and S.E. Shoelson. 2005. Local and systemic insulin resistance resulting from hepatic activation of IKK-beta and NF-kappaB. *Nat. Med.* 11:183-190. <https://doi.org/10.1038/nm1166>

Cai, J., K.M. Pires, M. Ferhat, B. Chaurasia, M.A. Buffolo, R. Smalling, A. Sargsyan, D.L. Atkinson, S.A. Summers, T.E. Graham, and S. Boudina. 2018. Autophagy Ablation in Adipocytes Induces Insulin Resistance and Reveals Roles for Lipid Peroxide and Nrf2 Signaling in Adipose-Liver Crosstalk. *Cell Rep.* 25:1708-1717.e5. <https://doi.org/10.1016/j.celrep.2018.10.040>

Chen, Q., E.J. Vazquez, S. Moghaddas, C.L. Hoppel, and E.J. Lesnefsky. 2003. Production of reactive oxygen species by mitochondria: central role of complex III. *J. Biol. Chem.* 278:36027-36031. <https://doi.org/10.1074/jbc.M304854200>

Collins, Y., E.T. Chouchani, A.M. James, K.E. Menger, H.M. Cocheme, and M.P. Murphy. 2012. Mitochondrial redox signalling at a glance. *J. Cell Sci.* 125:801-806. <https://doi.org/10.1242/jcs.098475>

Collins, J.A., S.T. Wood, K.J. Nelson, M.A. Rowe, C.S. Carlson, S. Chubinskaya, L.B. Poole, C.M. Furdai, and R.F. Loeser. 2016. Oxidative Stress Promotes Peroxiredoxin Hyperoxidation and Attenuates Pro-survival Signaling in Aging Chondrocytes. *J. Biol. Chem.* 291:6641-6654. <https://doi.org/10.1074/jbc.M115.693523>

Conrad, M., C. Jakupoglu, S.G. Moreno, S. Lippl, A. Banjac, M. Schneider, H. Beck, A.K. Hatzopoulos, U. Just, F. Sinowatz, et al. 2004. Essential role for mitochondrial thioredoxin reductase in hematopoiesis, heart development, and heart function. *Mol. Cell Biol.* 24:9414-9423. <https://doi.org/10.1128/MCB.24.21.9414-9423.2004>

Cypess, A.M., L.S. Weiner, C. Roberts-Toler, E. Franquet Elia, S.H. Kessler, P.A. Kahn, J. English, K. Chatman, S.A. Trauger, A. Doria, and G.M. Kolodny. 2015. Activation of human brown adipose tissue by a beta3-adrenergic receptor agonist. *Cell Metab.* 21:33-38. <https://doi.org/10.1016/j.cmet.2014.12.009>

Donath, M.Y., and S.E. Shoelson. 2011. Type 2 diabetes as an inflammatory disease. *Nat. Rev. Immunol.* 11:98-107. <https://doi.org/10.1038/nri2925>

Formentini, L., M. Sanchez-Arago, L. Sanchez-Cenizo, and J.M. Cuevas. 2012. The mitochondrial ATPase inhibitory factor 1 triggers a ROS-mediated retrograde pro-survival and proliferative response. *Mol. Cell.* 45:731-742. <https://doi.org/10.1016/j.molcel.2012.01.008>

Galluzzi, L., O. Kepp, C. Trojel-Hansen, and G. Kroemer. 2012. Mitochondrial control of cellular life, stress, and death. *Circ. Res.* 111:1198-1207. <https://doi.org/10.1161/CIRCRESAHA.112.268946>

Guilherme, A., J.V. Virbasius, V. Puri, and M.P. Czech. 2008. Adipocyte dysfunction linking obesity to insulin resistance and type 2 diabetes. *Nat. Rev. Mol. Cell Biol.* 9:367-377. <https://doi.org/10.1038/nrm2391>

Hajer, G.R., T.W. van Haften, and F.L. Visseren. 2008. Adipose tissue dysfunction in obesity, diabetes, and vascular diseases. *Eur. Heart J.* 29: 2959-2971. <https://doi.org/10.1093/eurheartj/ehn387>

He, W., Y. Barak, A. Hevener, P. Olson, D. Liao, J. Le, M. Nelson, E. Ong, J.M. Olefsky, and R.M. Evans. 2003. Adipose-specific peroxisome proliferator-activated receptor gamma knockout causes insulin resistance in fat and liver but not in muscle. *Proc. Natl. Acad. Sci. USA.* 100:15712-15717. <https://doi.org/10.1073/pnas.2536828100>

Heinonen, S., J. Buzkova, M. Muniandy, R. Kaksonen, M. Ollikainen, K. Ismail, A. Hakkarainen, J. Lundbom, N. Lundbom, K. Vuolteenaho, et al. 2015. Impaired Mitochondrial Biogenesis in Adipose Tissue in Acquired Obesity. *Diabetes.* 64:3135-3145. <https://doi.org/10.2337/db14-1937>

Herrmann, O., B. Baumann, R. de Lorenzi, S. Muhammad, W. Zhang, J. Kleesiek, M. Malfertheiner, M. Kohrmann, I. Petrovita, I. Maegle, et al. 2005. IKK mediates ischemia-induced neuronal death. *Nat. Med.* 11: 1322-1329. <https://doi.org/10.1038/nm1323>

Hotamisligil, G.S. 2017. Inflammation, metaflammation and immunometabolic disorders. *Nature.* 542:177-185. <https://doi.org/10.1038/nature21363>

Huang, Q., H.J. Zhou, H. Zhang, Y. Huang, F. Hinojosa-Kirschenbaum, P. Fan, L. Yao, L. Belardinelli, G. Tellides, F.J. Giordano, et al. 2015. Thioredoxin-2 inhibits mitochondrial reactive oxygen species generation and apoptosis stress kinase-1 activity to maintain cardiac function. *Circulation.* 131:1082-1097. <https://doi.org/10.1161/CIRCULATIONAHA.114.012725>

Jakupoglu, C., G.K. Przemec, M. Schneider, S.G. Moreno, N. Mayr, A.K. Hatzopoulos, M.H. de Angelis, W. Wurst, G.W. Bornkamm, M. Brielmeier, and M. Conrad. 2005. Cytoplasmic thioredoxin reductase is essential for embryogenesis but dispensable for cardiac development. *Mol. Cell Biol.* 25:1980-1988. <https://doi.org/10.1128/MCB.25.5.1980-1988.2005>

Janssen-Heininger, Y.M., M.E. Poynter, and P.A. Baeuerle. 2000. Recent advances towards understanding redox mechanisms in the activation of nuclear factor kappaB. *Free Radic. Biol. Med.* 28:1317-1327. [https://doi.org/10.1016/S0891-5849\(00\)00218-5](https://doi.org/10.1016/S0891-5849(00)00218-5)

Keller, M.P., and A.D. Attie. 2010. Physiological insights gained from gene expression analysis in obesity and diabetes. *Annu. Rev. Nutr.* 30: 341-364. <https://doi.org/10.1146/annurev.nutr.012809.104747>

Kiechl, S., J. Wittmann, A. Giaccari, M. Knoflach, P. Willeit, A. Bozec, A.R. Moschen, G. Muscogiuri, G.P. Sorice, T. Kireva, et al. 2013. Blockade of receptor activator of nuclear factor-kappaB (RANKL) signaling

- improves hepatic insulin resistance and prevents development of diabetes mellitus. *Nat. Med.* 19:358–363. <https://doi.org/10.1038/nm.3084>
- Kim, J.K., O. Gavrilova, Y. Chen, M.L. Reitman, and G.I. Shulman. 2000. Mechanism of insulin resistance in A-ZIP/F-1 fatless mice. *J. Biol. Chem.* 275:8456–8460. <https://doi.org/10.1074/jbc.275.12.8456>
- Kondegowda, N.G., R. Fenutria, I.R. Pollack, M. Orthofer, A. Garcia-Ocana, J.M. Penninger, and R.C. Vasavada. 2015. Osteoprotegerin and Denosumab Stimulate Human Beta Cell Proliferation through Inhibition of the Receptor Activator of NF-kappaB Ligand Pathway. *Cell Metab.* 22: 77–85. <https://doi.org/10.1016/j.cmet.2015.05.021>
- Kusminski, C.M., and P.E. Scherer. 2012. Mitochondrial dysfunction in white adipose tissue. *Trends Endocrinol. Metab.* 23:435–443. <https://doi.org/10.1016/j.tem.2012.06.004>
- Lee, S., S.M. Kim, and R.T. Lee. 2013. Thioredoxin and Thioredoxin Target Proteins: From Molecular Mechanisms to Functional Significance. *Antioxid. Redox Signal.* 18:1165–1207. <https://doi.org/10.1089/ars.2011.4322>
- Lotta, L.A., P. Gulati, F.R. Day, F. Payne, H. Ongen, M. van de Bunt, K.J. Gaulton, J.D. Eicher, S.J. Sharp, J. Luan, et al. 2017. Integrative genomic analysis implicates limited peripheral adipose storage capacity in the pathogenesis of human insulin resistance. *Nat. Genet.* 49:17–26. <https://doi.org/10.1038/ng.3714>
- Matsumoto, G., K. Wada, M. Okuno, M. Kurosawa, and N. Nukina. 2011. Serine 403 phosphorylation of p62/SQSTM1 regulates selective autophagic clearance of ubiquitinated proteins. *Mol. Cell.* 44:279–289. <https://doi.org/10.1016/j.molcel.2011.07.039>
- Matthews, J.R., N. Wakasugi, J.L. Virelizier, J. Yodoi, and R.T. Hay. 1992. Thioredoxin regulates the DNA binding activity of NF- κ B by reduction of a disulphid bond involving cysteine 62. *Nucleic Acids Res.* 20: 3821–3830. <https://doi.org/10.1093/nar/20.15.3821>
- Moon, H.S., M. Dalamaga, S.Y. Kim, S.A. Polyzos, O.P. Hamnvik, F. Magkos, J. Paruthi, and C.S. Mantzoros. 2013. Leptin's role in lipodystrophic and nonlipodystrophic insulin-resistant and diabetic individuals. *Endocr. Rev.* 34:377–412. <https://doi.org/10.1210/er.2012-1053>
- Morgan, M.J., and Z.G. Liu. 2011. Crosstalk of reactive oxygen species and NF-kappaB signaling. *Cell Res.* 21:103–115. <https://doi.org/10.1038/cr.2010.178>
- Mottillo, E.P., E.M. Desjardins, J.D. Crane, B.K. Smith, A.E. Green, S. Dummun, T.I. Henriksen, I.A. Rebalka, A. Razi, K. Sakamoto, et al. 2016. Lack of Adipocyte AMPK Exacerbates Insulin Resistance and Hepatic Steatosis through Brown and Beige Adipose Tissue Function. *Cell Metab.* 24:118–129. <https://doi.org/10.1016/j.cmet.2016.06.006>
- Narendra, D., L.A. Kane, D.N. Hauser, I.M. Fearney, and R.J. Youle. 2010. p62/SQSTM1 is required for Parkin-induced mitochondrial clustering but not mitophagy; VDAC1 is dispensable for both. *Autophagy.* 6: 1090–1106. <https://doi.org/10.4161/auto.6.8.13426>
- Nathan, C., and A. Cunningham-Bussell. 2013. Beyond oxidative stress: an immunologist's guide to reactive oxygen species. *Nat. Rev. Immunol.* 13: 349–361. <https://doi.org/10.1038/nri3423>
- Nonn, L., R.R. Williams, R.P. Erickson, and G. Powis. 2003. The absence of mitochondrial thioredoxin 2 causes massive apoptosis, exencephaly, and early embryonic lethality in homozygous mice. *Mol. Cell. Biol.* 23: 916–922. <https://doi.org/10.1128/MCB.23.3.916-922.2003>
- Oral, E.A., S.M. Reilly, A.V. Gomez, R. Meral, L. Butz, N. Ajluni, T.L. Cheverev, E. Koryntnaya, A.H. Neidert, R. Hench, et al. 2017. Inhibition of IKKe and TBK1 Improves Glucose Control in a Subset of Patients with Type 2 Diabetes. *Cell Metab.* 26:157–170.e7. <https://doi.org/10.1016/j.cmet.2017.06.006>
- Patil, N.K., N. Parajuli, L.A. MacMillan-Crow, and P.R. Mayeux. 2014. Inactivation of renal mitochondrial respiratory complexes and manganese superoxide dismutase during sepsis: mitochondria-targeted antioxidant mitigates injury. *Am. J. Physiol. Renal Physiol.* 306:F734–F743. <https://doi.org/10.1152/ajprenal.00643.2013>
- Patti, M.E., and S. Corvera. 2010. The role of mitochondria in the pathogenesis of type 2 diabetes. *Endocr. Rev.* 31:364–395. <https://doi.org/10.1210/er.2009-0027>
- Patti, M.E., A.J. Butte, S. Crunkhorn, K. Cusi, R. Berria, S. Kashyap, Y. Miyazaki, I. Kohane, M. Costello, R. Saccone, et al. 2003. Coordinated reduction of genes of oxidative metabolism in humans with insulin resistance and diabetes: Potential role of PGC1 and NRF1. *Proc. Natl. Acad. Sci. USA.* 100:8466–8471. <https://doi.org/10.1073/pnas.1032913100>
- Perry, R.J., J.G. Camporez, R. Kursawe, P.M. Titchenell, D. Zhang, C.J. Perry, M.J. Jurczak, A. Abudukadier, M.S. Han, X.M. Zhang, et al. 2015. Hepatic acetyl CoA links adipose tissue inflammation to hepatic insulin resistance and type 2 diabetes. *Cell.* 160:745–758. <https://doi.org/10.1016/j.cell.2015.01.012>
- Petersen, M.C., and G.I. Shulman. 2018. Mechanism of insulin action and insulin resistance. *Physiol. Rev.* 98:2133–2223. <https://doi.org/10.1152/physrev.00063.2017>
- Rutkowski, J.M., J.H. Stern, and P.E. Scherer. 2015. The cell biology of fat expansion. *J. Cell Biol.* 208:501–512. <https://doi.org/10.1083/jcb.201409063>
- Samuel, V.T., and G.I. Shulman. 2018. Nonalcoholic Fatty Liver Disease as a Nexus of Metabolic and Hepatic Diseases. *Cell Metab.* 27:22–41. <https://doi.org/10.1016/j.cmet.2017.08.002>
- Samuel, V.T., Z.X. Liu, A. Wang, S.A. Beddow, J.G. Geisler, M. Kahn, X.M. Zhang, B.P. Monia, S. Bhanot, and G.I. Shulman. 2007. Inhibition of protein kinase Cepsilon prevents hepatic insulin resistance in nonalcoholic fatty liver disease. *J. Clin. Invest.* 117:739–745. <https://doi.org/10.1172/JCI30400>
- Schroder, K., R. Zhou, and J. Tschopp. 2010. The NLRP3 inflammasome: a sensor for metabolic danger? *Science.* 327:296–300. <https://doi.org/10.1126/science.1184003>
- Shao, L., H.J. Zhou, H. Zhang, L. Qin, J. Hwa, Z. Yun, W. Ji, and W. Min. 2015. SENP1-mediated NEMO deSUMOylation in adipocytes limits inflammatory responses and type-1 diabetes progression. *Nat. Commun.* 6: 8917. <https://doi.org/10.1038/ncomms9917>
- Shulman, G.I. 2014. Ectopic fat in insulin resistance, dyslipidemia, and cardiometabolic disease. *N. Engl. J. Med.* 371:1131–1141. <https://doi.org/10.1056/NEJMr1011035>
- Smith, R.A., R.C. Hartley, H.M. Cocheme, and M.P. Murphy. 2012. Mitochondrial pharmacology. *Trends Pharmacol. Sci.* 33:341–352. <https://doi.org/10.1016/j.tips.2012.03.010>
- Stanley, B.A., V. Sivakumaran, S. Shi, I. McDonald, D. Lloyd, W.H. Watson, M.A. Aon, and N. Paolucci. 2011. Thioredoxin reductase-2 is essential for keeping low levels of H(2)O(2) emission from isolated heart mitochondria. *J. Biol. Chem.* 286:33669–33677. <https://doi.org/10.1074/jbc.M111.284612>
- Tanaka, T., F. Hosoi, Y. Yamaguchi-Iwai, H. Nakamura, H. Masutani, S. Ueda, A. Nishiyama, S. Takeda, H. Wada, G. Spyrrou, and J. Yodoi. 2002. Thioredoxin-2 (TRX-2) is an essential gene regulating mitochondria-dependent apoptosis. *EMBO J.* 21:1695–1703. <https://doi.org/10.1093/emboj/21.7.1695>
- Tang, Y., M. Wallace, J. Sanchez-Gurmaches, W.Y. Hsiao, H. Li, P.L. Lee, S. Vernia, C.M. Metallo, and D.A. Guertin. 2016. Adipose tissue mTORC2 regulates ChREBP-driven de novo lipogenesis and hepatic glucose metabolism. *Nat. Commun.* 7:11365. <https://doi.org/10.1038/ncomms11365>
- Vatner, D.F., S.K. Majumdar, N. Kumashiro, M.C. Petersen, Y. Rahimi, A.K. Gattu, M. Bears, J.P. Camporez, G.W. Cline, M.J. Jurczak, et al. 2015. Insulin-independent regulation of hepatic triglyceride synthesis by fatty acids. *Proc. Natl. Acad. Sci. USA.* 112:1143–1148. <https://doi.org/10.1073/pnas.1423952112>
- Vernochet, C., A. Mourier, O. Bezy, Y. Macotela, J. Boucher, M.J. Rardin, D. An, K.Y. Lee, O.R. Ilkayeva, C.M. Zingaretti, et al. 2012. Adipose-specific deletion of TFAM increases mitochondrial oxidation and protects mice against obesity and insulin resistance. *Cell Metab.* 16:765–776. <https://doi.org/10.1016/j.cmet.2012.10.016>
- Vernochet, C., F. Damilano, A. Mourier, O. Bezy, M.A. Mori, G. Smyth, A. Rosenzweig, N.G. Larsson, and C.R. Kahn. 2014. Adipose tissue mitochondrial dysfunction triggers a lipodystrophic syndrome with insulin resistance, hepatosteatosis, and cardiovascular complications. *FASEB J.* 28:4408–4419. <https://doi.org/10.1096/fj.14-253971>
- Wellen, K.E., and G.S. Hotamisligil. 2005. Inflammation, stress, and diabetes. *J. Clin. Invest.* 115:1111–1119. <https://doi.org/10.1172/JCI25102>
- Wilson-Fritch, L., S. Nicoloso, M. Chouinard, M.A. Lazar, P.C. Chui, J. Leszyk, J. Straubhaar, M.P. Czech, and S. Corvera. 2004. Mitochondrial remodeling in adipose tissue associated with obesity and treatment with rosiglitazone. *J. Clin. Invest.* 114:1281–1289. <https://doi.org/10.1172/JCI21752>
- Yamamoto, M., E. Yamato, S. Toyoda, F. Tashiro, H. Ikegami, J. Yodoi, and J. Miyazaki. 2008. Transgenic expression of antioxidant protein thioredoxin in pancreatic beta cells prevents progression of type 2 diabetes mellitus. *Antioxid. Redox Signal.* 10:43–50. <https://doi.org/10.1089/ars.2007.1586>
- Yang, Q., T.E. Graham, N. Mody, F. Preitner, O.D. Peroni, J.M. Zabolotny, K. Kotani, L. Quadro, and B.B. Kahn. 2005. Serum retinol binding protein 4 contributes to insulin resistance in obesity and type 2 diabetes. *Nature.* 436:356–362. <https://doi.org/10.1038/nature03711>
- Yoshioka, J., W.A. Chutkow, S. Lee, J.B. Kim, J. Yan, R. Tian, M.L. Lindsey, E.P. Feener, C.E. Seidman, J.G. Seidman, and R.T. Lee. 2012. Deletion of

- thioredoxin-interacting protein in mice impairs mitochondrial function but protects the myocardium from ischemia-reperfusion injury. *J. Clin. Invest.* 122:267–279. <https://doi.org/10.1172/JCI44927>
- Zhang, Y., S. Goldman, R. Baerga, Y. Zhao, M. Komatsu, and S. Jin. 2009. Adipose-specific deletion of autophagy-related gene 7 (*atg7*) in mice reveals a role in adipogenesis. *Proc. Natl. Acad. Sci. USA.* 106:19860–19865. <https://doi.org/10.1073/pnas.0906048106>
- Zhang, D., J. Christianson, Z.X. Liu, L. Tian, C.S. Choi, S. Neschen, J. Dong, P.A. Wood, and G.I. Shulman. 2010. Resistance to high-fat diet-induced obesity and insulin resistance in mice with very long-chain acyl-CoA dehydrogenase deficiency. *Cell Metab.* 11:402–411. <https://doi.org/10.1016/j.cmet.2010.03.012>
- Zhao, P., K.I. Wong, X. Sun, S.M. Reilly, M. Uhm, Z. Liao, Y. Skorobogatko, and A.R. Saltiel. 2018. TBK1 at the Crossroads of Inflammation and Energy Homeostasis in Adipose Tissue. *Cell.* 172:731–743.e12. <https://doi.org/10.1016/j.cell.2018.01.007>
- Zhong, Z., A. Umemura, E. Sanchez-Lopez, S. Liang, S. Shalapour, J. Wong, F. He, D. Boassa, G. Perkins, S.R. Ali, et al. 2016. NF-kappaB Restricts Inflammasome Activation via Elimination of Damaged Mitochondria. *Cell.* 164:896–910. <https://doi.org/10.1016/j.cell.2015.12.057>
- Zhou, H.J., L. Qin, H. Zhang, W. Tang, W. Ji, Y. He, X. Liang, Z. Wang, Q. Yuan, A. Vortmeyer, et al. 2016. Endothelial exocytosis of angiopoietin-2 resulting from CCM3 deficiency contributes to cerebral cavernous malformation. *Nat. Med.* 22:1033–1042. <https://doi.org/10.1038/nm.4169>

Supplemental material

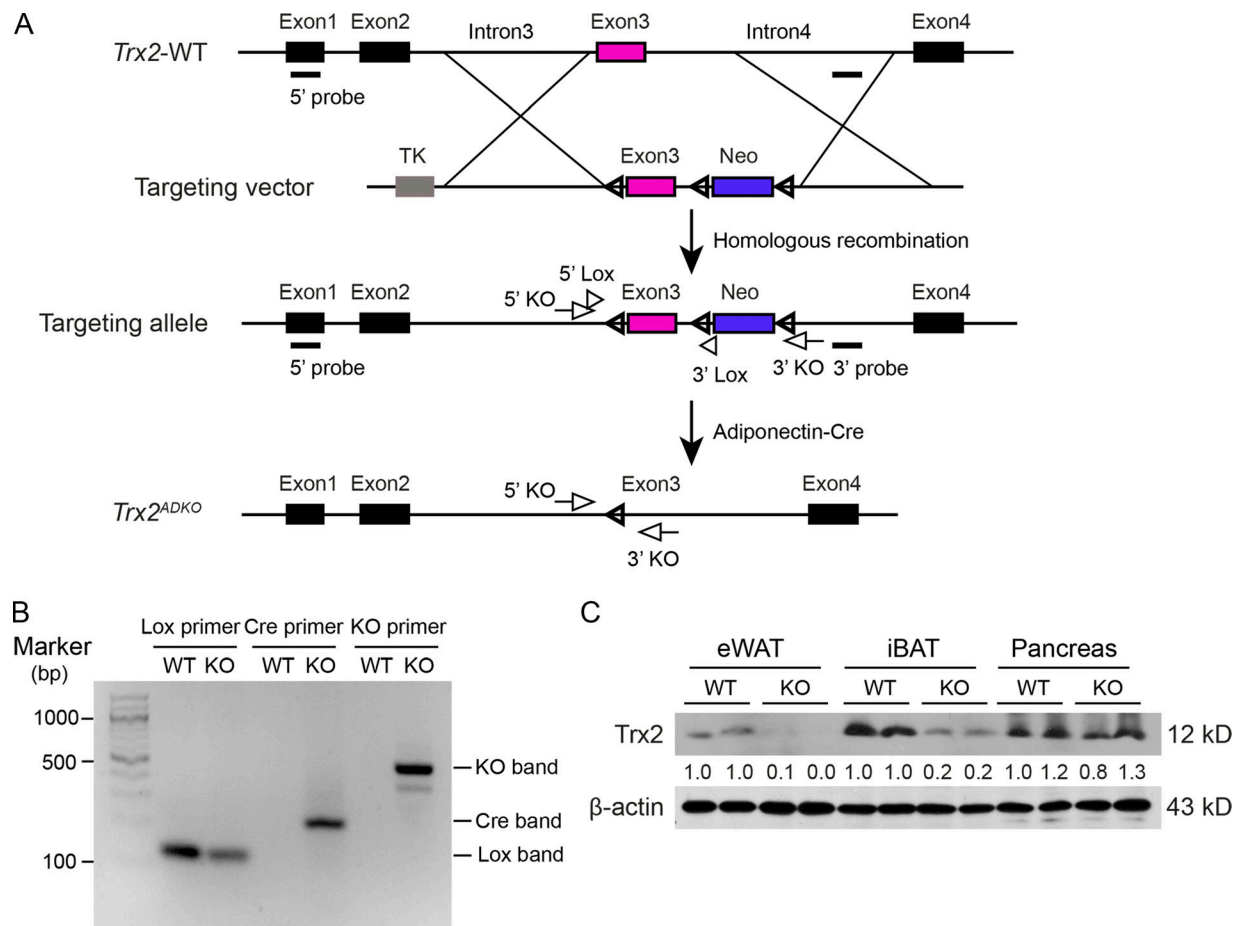


Figure S1. **Trx2** targeting strategy and adipocyte-specific deletion. **(A)** Schematic diagram of adipocyte-specific *Trx2* KO by the loxP-Cre system. **(B)** Genotyping results of *Trx2*^{lox/lox} (WT) and *Trx2*^{ADKO} (*Trx2*^{lox/lox}; Adipo-Cre; KO) mice. Note that WT mice did not contain Cre. **(C)** Representative Western blot analysis of *Trx2* expression in eWAT, interscapular BAT (iBAT), and pancreas from WT and KO mice. β-Actin was used as a loading control. TK, thymidine kinase.

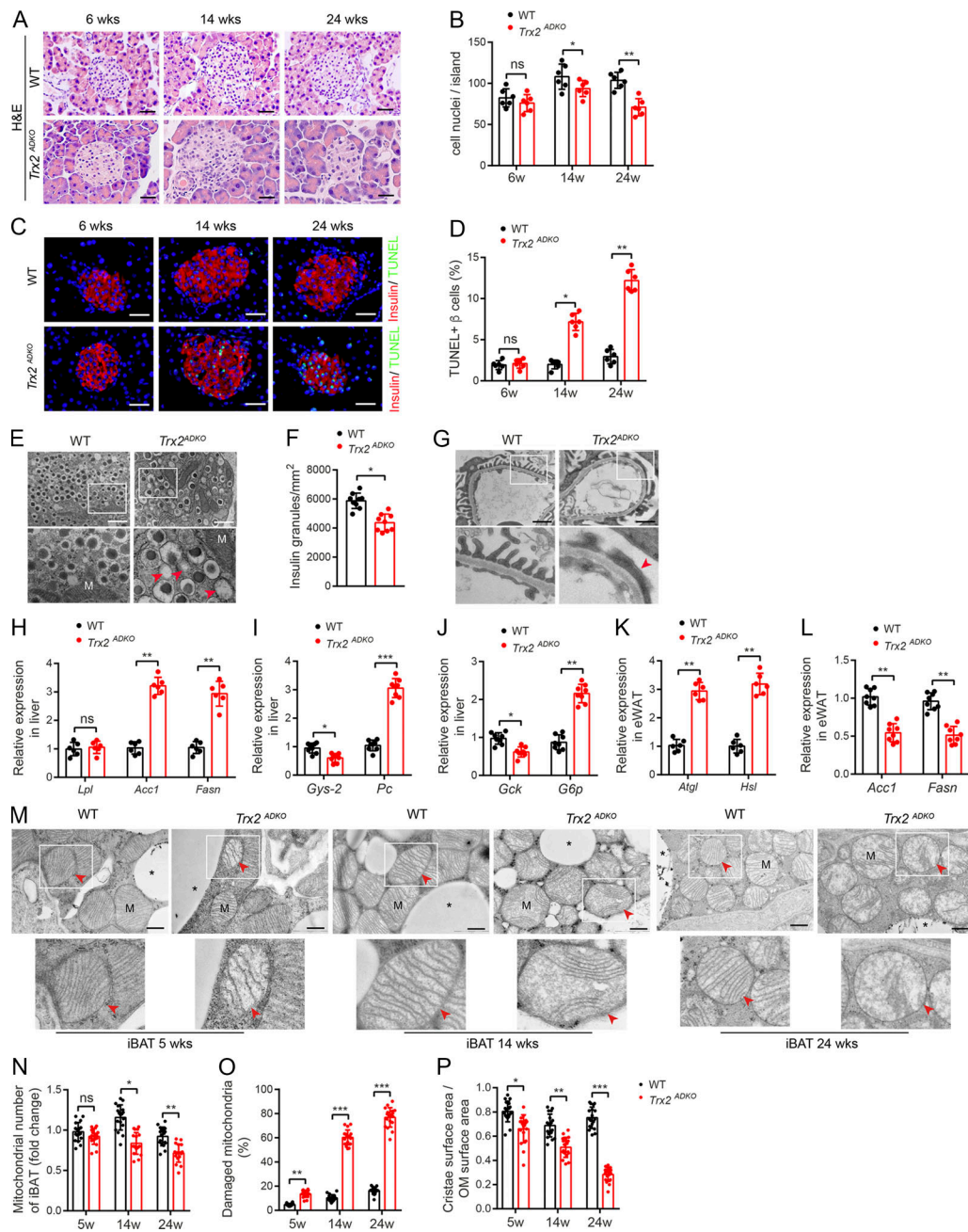


Figure S3. *Trx2^{ADKO}* mice develop T2DM-related end-organ damage. (A–E) *Trx2*-KO mice exhibit decreased insulin content and increased β cell apoptosis. (A) Representative hematoxylin and eosin–stained pancreas sections showing pancreatic islets of WT and *Trx2^{ADKO}* mice at the indicated ages. Scale bars, 20 μm. (B) Nuclei density of six randomly selected pancreatic islets (*n* = 6 mice). (C) Detection of β cell apoptosis by costaining of TUNEL (green) and insulin (red). Representative images from WT and *Trx2^{ADKO}* mice at the indicated ages. Scale bars, 20 μm. (D) Quantification of TUNEL-positive β cells (right panel; *n* = 6 mice). (E) Representative transmission electron micrographs of pancreas tissue from WT and *Trx2^{ADKO}* mice (three images/mouse, *n* = 3 mice/group). Squares correspond to the magnified areas (bottom panel). Scale bars, 1 μm. M, mitochondria. Arrowheads indicate empty granules. (F) Quantification of insulin granules per μm² islet. (G) Representative transmission electron micrographs of kidney tissue from WT and *Trx2^{ADKO}* mice (*n* = 3). White squares correspond to the magnified areas (bottom panel). Red arrowhead indicates podocyte foot process fusion. Scale bars, 1 μm. (H–L) Quantitative analysis of de novo lipogenesis and hepatic gluconeogenic genes. (H) Relative mRNA expression of lipogenesis genes in liver in 14-wk-old male WT and *Trx2^{ADKO}* mice (*n* = 6). (I and J) Relative mRNA expression of hepatic gluconeogenic genes in liver of 14-wk-old male WT and *Trx2^{ADKO}* mice (*n* = 8). (K) Relative mRNA expression of the indicated de novo lipogenesis genes in eWAT of 14-wk-old male WT and *Trx2^{ADKO}* mice (*n* = 8). (L) Relative mRNA expression of lipolysis genes in eWAT in 14-wk-old male WT and *Trx2^{ADKO}* mice (*n* = 6). Quantitative data represent the mean ± SEM. ns, not significant; **, *P* < 0.01; ***, *P* < 0.001 compared with WT controls (two-tailed Student's *t* test). *Acc*, acetyl-CoA carboxylase 1; *Atgl*, adipose TG lipase; *Fasn*, fatty acid synthase; *G6p*, glucose 6-phosphatase; *Gck*, glucokinase; *Gys2*, glycogen synthase 2; *Hsl*, hormone-sensitive lipase; *Lpl*, lipoprotein lipase; *Pc*, pyruvate carboxylase. (M–P) TEM analysis of brown adipose mitochondria. (M) Representative transmission electron micrographs of interscapular BAT (iBAT) sections from WT and *Trx2^{ADKO}* mice at the indicated ages. Asterisks indicate LDs. Squares correspond to the magnified areas (bottom panel). Arrowheads indicate mitochondria. Scale bars, 0.5 μm. (N–P) Number of mitochondria, number of damaged mitochondria, and cristae surface area/outer membrane (OM) surface area (six images/mouse; *n* = 3 mice/group). Quantitative data represent the mean ± SEM. ns, not significant; *, *P* < 0.05; **, *P* < 0.01; ***, *P* < 0.001 versus WT (two-tailed Student's *t* test). w, weeks.

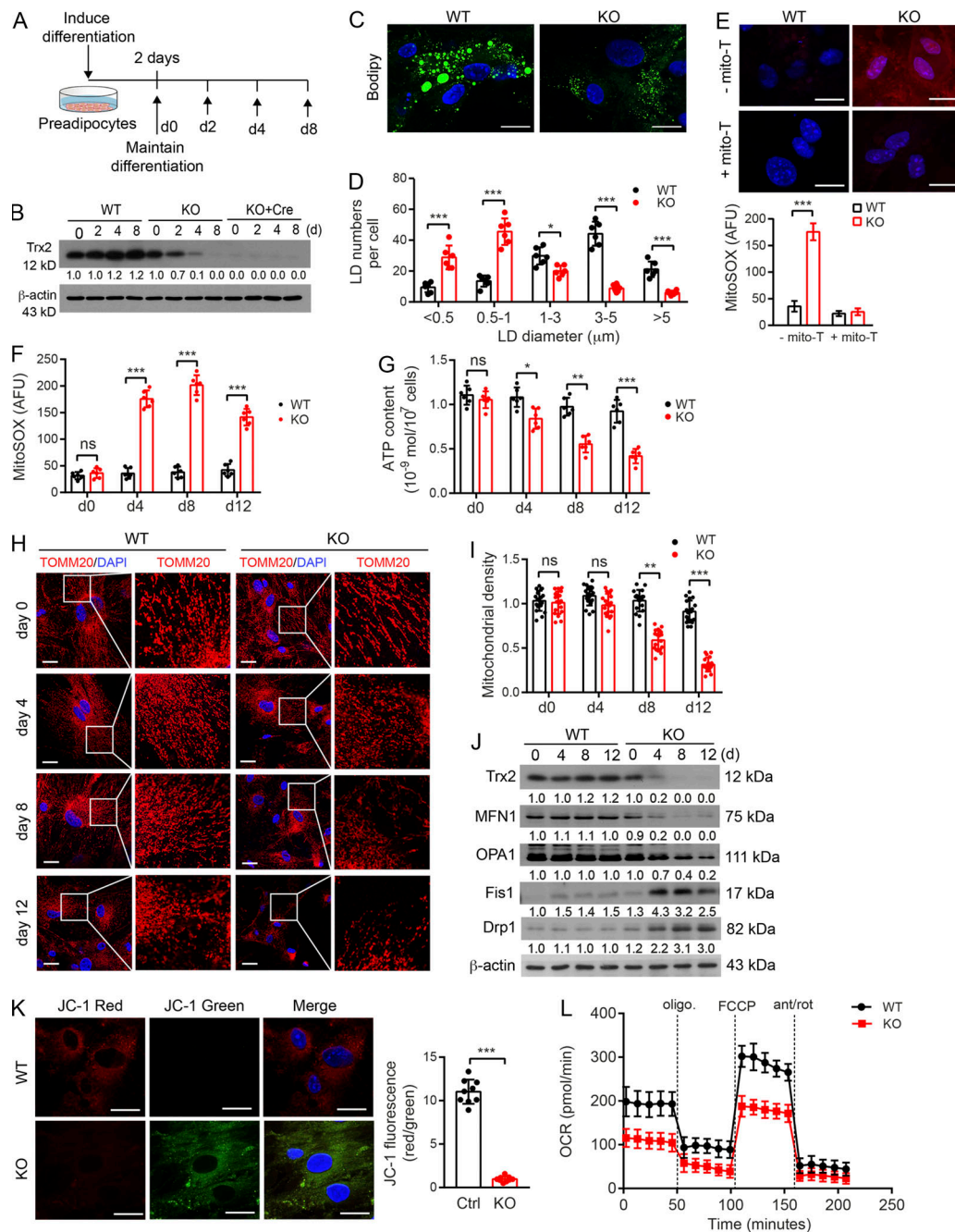


Figure S4. *Trx2* deficiency increases ROS in isolated adipocytes and alters mitochondrial energetics and oxidative metabolism. (A–D) *TRX2* deficiency reduces lipogenesis during preadipocytes differentiation. **(A)** Differentiation scheme of preadipocytes isolated from eWAT of WT (*Trx2^{lox/lox}*) and *Trx2^{ADKO}* (KO) mice. **(B)** Representative Western blots confirming a decrease of *TRX2* expression in *Trx2^{ADKO}* adipocytes during differentiation upon Adipo-Cre was activated on day 4. Adeno-Cre infection rapidly induced *Trx2* deletion. Protein levels were quantified and are presented as fold changes by taking WT as 1.0. *n* = 3. **(C and D)** Representative BODIPY staining images of WT and KO differentiated adipocytes at day 8 (C) and LD sizes (D) from six random fields were quantified (*n* = 3 biological repeats). **(E)** Representative micrographs of mitochondrial ROS levels by the mitoSOX staining of WT and *Trx2^{ADKO}* (KO) differentiated adipocytes at day 4 in the presence or absence of mito-TEMPO (*n* = 3). **(F)** Quantification of mitochondrial ROS levels of WT and KO differentiated adipocytes at different time points (*n* = 3). AFU, arbitrary fluorescence unit. **(G)** ATP content of mitochondria from WT and KO adipocytes during differentiation (*n* = 6). **(H and I)** Confocal fluorescence images showing mitochondrial dynamics stained with TOMM20 antibody (H) and quantified mitochondrial density via fluorescence intensity (I; six images/mouse, *n* = 3 mice/group). **(J)** Western blot analysis of mitochondrial fusion mediators MFN1 and OPA1, fusion mediators Drp1 and Fis1 from WT and KO adipocytes at different differentiation time points. Protein levels were quantified and presented as fold changes by taking WT as 1.0 (*n* = 3). **(K)** *Trx2* deletion in adipocytes decreased mitochondrial membrane potential. Mitochondrial membrane potential ($\Delta\Psi$ m) was assessed with the JC-1 probe by confocal microscopy at day 4 (left panel) and quantified by a red to green fluorescence intensities ratio (right panel). Scale bars, 20 μ m. Data are representative of three experiments in 10 randomly selected fields from each group (*n* = 3). Ctrl, control. **(L)** The oxygen consumption rate (OCR) of WT and KO differentiated adipocytes measured by Seahorse at day 4 (*n* = 3). Quantitative data are presented as mean \pm SEM. ns, not significant; *, *P* < 0.05; **, *P* < 0.01; ***, *P* < 0.001 versus the corresponding value for control. Significance was analyzed by two-tailed Student's *t* test. Scale bars, 20 μ m (C, E, H, and K). FCCP, carbonyl cyanide-4-(trifluoromethoxy)phenylhydrazone.

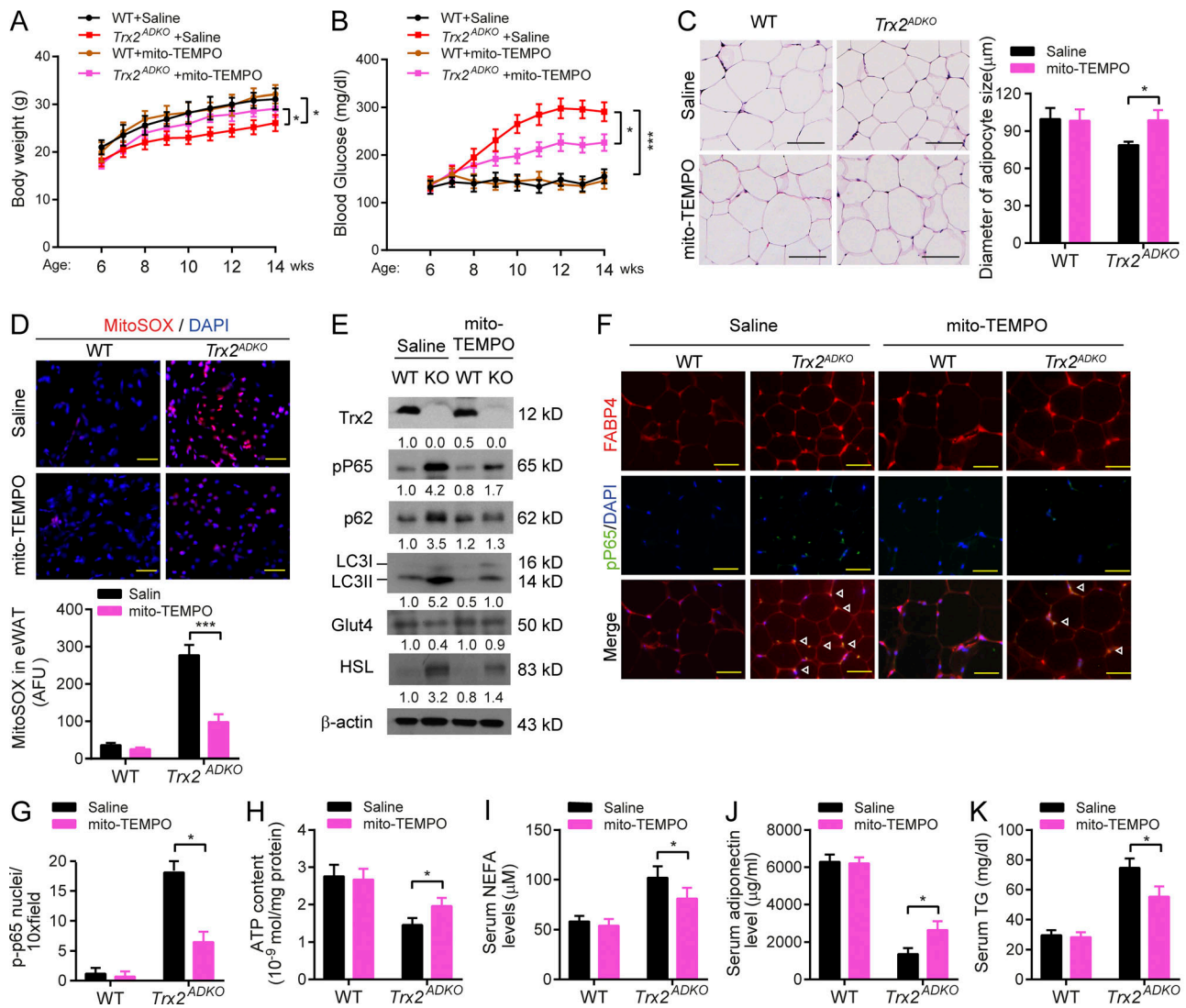


Figure S5. **Mitochondria-specific antioxidant mito-TEMPO ameliorates adipocyte dysfunction and T2DM in *Trx2^{ADKO}* mice.** WT and *Trx2^{ADKO}* mice at age of 6 wk received injections of mito-TEMPO (0.7 mg/kg/d, i.p. every other day) or vehicle (saline) for 8 wk. Body weight and blood glucose levels were measured at various ages and mouse tissues were harvested at week 14 for analyses. **(A and B)** Body weight (A) and fasting blood glucose levels (B) of mice at the indicated ages ($n = 8$ per group). **(C)** Representative hematoxylin and eosin staining showing overall eWAT morphology and adipocyte size in eWAT ($n = 3$ per group). **(D)** ROS analysis was performed by immunofluorescence microscopy of mitoSOX-stained eWAT, and quantification of fluorescence intensity with and without mito-TEMPO treatment. AFU, arbitrary fluorescence unit ($n = 3$ per group). **(E)** Immunoblot analysis of eWAT tissues ($n = 3$ per group). Protein levels were quantified and presented as fold changes by taking WT as 1.0. $n = 3$ mice for each group. **(F and G)** Coimmunostaining of phospho-P65 (green) and FABP4 (red) in eWAT sections. Representative images are shown in F with quantifications in G. $n = 3$ per group. White arrowheads indicate phospho-P65 in the nucleus. **(H)** ATP content of mitochondria isolated from eWAT of mice ($n = 6$ per group). **(I–K)** Plasma levels of NEFA (I), adiponectin (J), and TG (K; $n = 8$ per group). *, $P < 0.05$; ***, $P < 0.001$ (one-way ANOVA followed by Tukey's post hoc test). Scale bars, 20 μm (C), 100 μm (D), and 50 μm (F).

Provided online are two tables. Table S1 lists anthropometric and clinical variables of the study subjects. Table S2 lists primer sequences used for real-time PCR analysis.